



**UNIVERSIDADE DE SÃO PAULO**  
ESCOLA DE ENGENHARIA DE SÃO CARLOS  
DEPARTAMENTO DE ENGENHARIA ELÉTRICA E DE COMPUTAÇÃO

**Dissertação de Mestrado**

*Systematic comparison between photonic sensors based on dielectrics  
and metals*

MESTRE EM CIÊNCIAS, Programa de Engenharia Elétrica: Rodrigo Romão França Soares  
ORIENTADOR: Prof. Dr. Emiliano Rezende Martins

São Carlos  
2020

**Trata-se da versão corrigida da dissertação. A versão original se encontra disponível na EESC/USP que aloja o Programa de Pós-Graduação de Engenharia Elétrica.**

RODRIGO ROMÃO FRANÇA SOARES

SYSTEMATIC COMPARISON BETWEEN PHOTONIC SENSORS BASED ON  
DIELECTRICS AND METALS

Dissertação apresentada à Escola  
de Engenharia de São Carlos para a  
obtenção do título de Mestre em  
Ciências

Área de Concentração:  
Telecomunicações

Orientador: Prof. Dr. Emiliano  
Rezende Martins

São Carlos

2020

AUTORIZO A REPRODUÇÃO TOTAL OU PARCIAL DESTE TRABALHO, POR QUALQUER MEIO CONVENCIONAL OU ELETRÔNICO, PARA FINS DE ESTUDO E PESQUISA, DESDE QUE CITADA A FONTE.

Ficha catalográfica elaborada pela Biblioteca Prof. Dr. Sérgio Rodrigues Fontes da EESC/USP com os dados inseridos pelo(a) autor(a).

S676s	<p>Soares, Rodrigo Romão França</p> <p>Systematic comparison between photonic sensors based on dielectrics and metals / Rodrigo Romão França Soares; orientador Emiliano Rezende Martins. São Carlos, 2020.</p> <p>Dissertação (Mestrado) - Programa de Pós-Graduação em Engenharia Elétrica e Área de Concentração em Telecomunicações -- Escola de Engenharia de São Carlos da Universidade de São Paulo, 2020.</p> <p>1. Photonics. 2. Biosensing. 3. Dielectric media. 4. Plasmonics. 5. Biophotonics. I. Título.</p>
-------	---

Eduardo Graziosi Silva - CRB - 8/8907

## FOLHA DE JULGAMENTO

Candidato: Engenheiro **RODRIGO ROMÃO FRANÇA SOARES**.

Título da dissertação: "Comparação sistêmica entre sensores fotônicos baseados em dielétricos e metais".

Data da defesa: 15/05/2020

### Comissão Julgadora:

### Resultado:

Prof. Dr. **Emiliano Rezende Martins**  
**(Orientador)**  
(Escola de Engenharia de São Carlos/EESC-USP)

**APROVADO**

Prof. Dr. **Luís Alberto Mijam Barêa**  
(Universidade Federal de São Carlos/UFSCar)

**APROVADO**

Prof. Dr. **Filippo Giovanni Ghiglieno**  
(Universidade Federal de São Carlos/UFSCar)

**APROVADO**

Coordenador do Programa de Pós-Graduação em Engenharia Elétrica:  
Prof. Titular **Ivan Nunes da Silva**

Presidente da Comissão de Pós-Graduação:  
Prof. Titular **Murilo Araujo Romero**

For all the support, company, resilience, and above all love,  
I dedicate this work for you, my dearest Nadyne

## **AGRADECIMENTOS**

Aqui gostaria de dedicar um sincero agradecimento às pessoas que foram fundamentais durante esse período. Primeiramente, a Deus pela dádiva da vida. Em segundo lugar à Nadyne, minha companheira, pelo apoio incondicional em todos os momentos dos felizes aos difíceis durante essa jornada. A minha mãe e minha família por terem me ensinado que a educação é o único caminho possível. Em especial ao meu orientador Emiliano Rezende pela compreensão em primeiro lugar, pelo apoio e pelo exemplo de competência, dedicação e vocação, o senhor é sem dúvidas a pessoa mais inteligente com quem convive, muito obrigado pelo tempo que dedicou ao meu aprendizado e a este trabalho. Aos amigos do Lab de Telecom, sinto falta dos finais de tarde as cantorias desafinadas que ia de sertanejo raiz a Raul Seixas, obrigado especial ao Augusto, simplesmente um gênio, e ao Mateuzinho, o grande gente fina. Achilles, Fabricio, Vinicius, Rodrigo e Michel, obrigado pela convivência. Por fim, agradeço ao povo Brasileiro que através da CAPES financiou por meio de bolsa de Mestrado durante o ano de 2018 este trabalho, muito obrigado.

A gente tem que ter coragem para  
enfrentar os desafios da vida.

João Victor

## **ABSTRACT**

SOARES, R. R. F. **Systematic comparison between photonic sensors based on dielectrics and metals.** 2020. Dissertação (Mestrado em Ciência) - Departamento de Engenharia Elétrica e de Computação, Universidade de São Paulo, São Carlos, 2020.

Photonic biosensors have gained much attention recently due to their high sensitivity, low energy consumption and miniaturization capability; in the near future, these sensors will form the basis of the so-called Lab on a Chip: a device capable of performing accurate clinical analyzes in a single chip and in any location, being of great help in countries with few resources for disease detection. There are several configurations for biophotonic sensors ranging from fiber-optic based systems, waveguides, resonators, to nanoparticles and photonic crystals, to name a few. In spite of this great diversity, constituted by dielectric or metallic media, these devices can be classified in two broad categories: those that require previous mode coupling and those that do not. The purpose of this dissertation is to study the devices of the second category, focusing on the so-called quasi-guided modes, presenting the physical phenomena involved and the main tools used to evaluate their performances. Therefore, using numerical simulations, present a comparative study between dielectric and metallic systems. Finally, a dielectric based biosensor is proposed, aiming on obtaining the similar performances of devices based on metal.

**Keywords:** Photonics. Biosensors. Systemic comparison.



## **RESUMO**

SOARES, R. R. F. **Comparação sistêmica entre sensores fotônicos baseados em dielétricos e metais.** 2020. Dissertação (Mestrado em Ciência) - Departamento de Engenharia Elétrica e de Computação, Universidade de São Paulo, São Carlos, 2020.

Biosensores fotônicos tem ganhado muita atenção recentemente devido a sua alta sensibilidade, baixo consumo de energia e capacidade de miniaturização; em um futuro próximo, esses sensores formarão a base do chamado Laboratório em um chip: um dispositivo capaz de executar com acurácia análises clínicas em um único chip e em qualquer local, sendo de grande ajuda a países com recursos escassos na detecção de doenças. Existem diversas configurações de sensores biofotônicos, variando desde sistemas baseados em fibras-ópticas, guias de onda, ressonadores, até nanopartículas e cristais fotônicos, para nomear alguns. Apesar de sua grande diversidade, constituindo-se por meios dielétricos ou metálicos, esses dispositivos podem ser classificados, de modo geral, em duas categorias: os que requerem acoplamento prévio do modo e aquelas de não requerem. O intuito dessa dissertação é estudar esses dispositivos da segunda categoria, focando nos chamados modos quase-guiados, apresentando os fenômenos físicos envolvidos e as principais ferramentas de avaliação da sua performance. Portanto, utilizando de simulações numéricas, apresentar um estudo comparativo entre os sistemas dielétricos e metálicos. Por fim, propor um biosensor baseado em meio dielétrico, com objetivo de atingir rendimento similar aos dispositivos baseados em metais.

**Palavras-chave:** Fotônica. Biosensores. Comparação Sistêmica.

## LIST OF FIGURES

<b>Figure 1-1</b> – Thermostat .....	1
<b>Figure 1-2</b> – Schematic of a biosensor .....	2
<b>Figure 1-3</b> – Spectrum change due to refractive index variation.....	4
<b>Figure 1-4</b> – Two Classes of Photonic Systems .....	5
<b>Figure 2-1</b> – Quasi-static approximation .....	10
<b>Figure 2-2</b> – Small sphere in a uniform electric field.....	11
<b>Figure 2-3</b> – Dipole moment induce from an external field .....	12
<b>Figure 2-4</b> – Simulation of a LSPR mode on resonance .....	13
<b>Figure 2-5</b> – Ray optics description.....	15
<b>Figure 2-6</b> – Total internal reflection.....	16
<b>Figure 2-7</b> – TE and TM Polarizations,.....	16
<b>Figure 2-8</b> – Slab Waveguide .....	17
<b>Figure 2-9</b> – Waveguide dispersion.....	19
<b>Figure 2-10</b> – Waveguide modes.....	19
<b>Figure 2-11</b> – Surface Wave .....	20
<b>Figure 2-12</b> – Grating. ....	22
<b>Figure 2-13</b> – Bragg Law.....	23
<b>Figure 2-14</b> – Waveguide mode coupling through a grating.....	24
<b>Figure 2-15</b> – Dispersion plot and mode coupling .....	25
<b>Figure 2-16</b> – Resonance shift caused by medium perturbation.....	26
<b>Figure 3-1</b> - Au Nanoholes structure .....	29
<b>Figure 3-2</b> – Dispersion of the SPR.....	30
<b>Figure 3-3</b> – Transmittance Nanogold array structure.....	31
<b>Figure 3-4</b> – Field Profile at resonance.....	31
<b>Figure 3-5</b> – Dispersion of the SPR modes .....	32
<b>Figure 3-6</b> - Transmittance Nanogold array structure .....	33
<b>Figure 3-7</b> – SOI nanohole array photonic crystal.....	34
<b>Figure 3-8</b> – Dispersion plot (SOI).....	35
<b>Figure 3-9</b> – Fano resonance of the sensor. ....	35
<b>Figure 3-10</b> – Field Profile at resonance.....	36
<b>Figure 4-1</b> – Amorphous Silicon Refractive Index (n, k).....	38
<b>Figure 4-2</b> – Dispersion diagram .....	39

<b>Figure 4-3</b> – Biosensor Parameters. ....	39
<b>Figure 4-4</b> – Transmittance response .....	40
<b>Figure 4-5</b> – Biosensor’s Fields Profiles.....	41
<b>Figure 4-6</b> – Influence of $\Lambda$ on the Spectral Response.....	42
<b>Figure 4-7</b> – Influence of $td$ on the Spectral Response .....	42
<b>Figure 4-8</b> – Influence of $td$ – transition from Fano to Lorentz resonance .....	43
<b>Figure 4-9</b> – Influence of the hole parameter (a) radius – $r$ and (b) depth of etching – $de$ ....	43
<b>Figure 4-10</b> – Relation between $SB$ and $\Lambda$ .....	44
<b>Figure 4-11</b> – Final Design – a-Si nanohole array photonic crystal .....	45
<b>Figure 4-12</b> – Transmittance response of the sensor.....	45
<b>Figure 4-13</b> – Field Profile of TM-like Mode.....	45

## LIST OF TABLES

<b>Table 1</b> – Waveguide-based photonic biosensors technologies.....	7
<b>Table 2</b> – Free space coupling based photonic biosensors technologies .....	8
<b>Table 3</b> – Sensors Comparison: Plasmonic based on Au vs Dielectric based on SOI.....	36
<b>Table 4</b> – Sensors Comparison: Au vs SOI vs a-Si (initial design).....	41
<b>Table 5</b> – Influence of sensor’s parameters on Bulk Sensitivity .....	44
<b>Table 6</b> – Sensors Comparison: Au vs SOI vs a-Si (final design).....	46

## LIST OF SYMBOLS

a-Si	Amorphous Silicon
$\theta$	Angle
$m$	Arbitrary integer
$S_B$	Bulk Sensitivity
$\tau$	Decay time
D	Dielectric
$E_d$	Dissipated Energy
$P_d$	Dissipated Power
$n_{eff}$	Effective Refractive Index
$\mathbf{E}$	Electric Field Vector
$\varphi$	Electrostatic Potential
$U$	Energy
FOM	Figure-of-merit
FDTD	Finite Difference Time Domain
$\mathbf{c}$	Fourier Series Coefficient
$k_0$	Free-space wavenumber
FWHM	Fullwidth Half Maximum
Au	Gold
$\Lambda$	Grating Period
$\mathbf{G}$	Grating Vector
GMR	Guided Mode Resonance
$\mathbf{p}$	Induce Dipole Moment Vector
IoT	Internet of Things
IPA	Isopropanol
LoC	Lab-on-a-chip
$\nabla^2$	Laplacian operator
$l$	Length
$\Delta l$	Length Variation
LED	Light Emitting Diodes
LOD	Limit of Detection
$\Delta\omega$	Linewidth
LSPR	Localized Surface Plasmon Resonance
$\mathbf{H}$	Magnetic Field Vector
M	Metallic
$\mu\text{g}$	Micrograms
ml	Milliliters
ng	Nanograms
NHA	Nanohole Arrays
$T$	Period

$\epsilon$	Permittivity or dielectric constant
$\phi$	Phase shift
PhC	Photonic Crystals
pg	Picograms
POC	Point-of-care
$\beta$	Propagation Constant
Q	Quality Factor
QGM	Quasi-guided modes
RI	Refractive Index
$n$	Refractive Index
RIU	Refractive Index Unity
$\Delta n$	Refractive Index variation
$\omega_0$	Resonance Angular Frequency
$\lambda_0$	Resonance wavelength
RCWA	Rigorous Coupled Wave Analysis
SOI	Silicon on Insulator
$a$	Spherical radius
SPR	Surface Plasmon Resonance
$S_s$	Surface Sensitivity
$\Delta T$	Thermal Variation
$d$	Thickness
TIR	Total Internal Reflection
TE	Transverse Electric
TM	Transverse Magnetic
$\epsilon_0$	Vacuum Permittivity
$\lambda$	Wavelength
$\Delta\lambda$	Wavelength variation
$k$	Wavevector

## SUMMARY

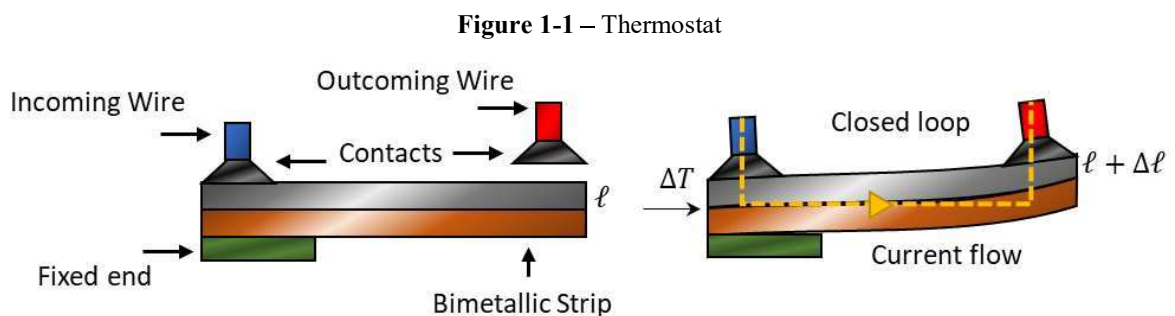
1.	Introduction .....	1
1.1	What is sensing? .....	1
1.2	Photonics in biosensing .....	4
1.3	Objective and Text structure .....	9
2	Physical Concepts .....	10
2.1	Localized modes .....	10
2.2	Guided modes .....	15
2.2.1	Slab waveguide .....	17
2.2.2	Surface Modes .....	20
2.3	Quasi-guided modes .....	22
2.4	Quasi-guided modes in biosensing .....	26
2.5	Sensing Parameters .....	27
3	Dielectric versus Metallic based media Sensors .....	29
3.1	Nanohole Arrays – Metallic Based Biosensors .....	29
3.2	Nanohole Arrays – Dielectric Based Biosensor .....	34
4	Dielectric Biosensor based on a-Si .....	37
4.1	Amorphous Silicon (a-Si) .....	37
4.2	Design of the a-Si Biosensor .....	38
5	Conclusions .....	46
6	References .....	47

# 1. INTRODUCTION

## 1.1 What is sensing?

Sensors pervade modern life: from a simple light bulb that turns on and off depending on whether there is anybody in the room, to a space rover on Mars that measures the chemical compounds of the planet's atmosphere. The first sensor dates back to the XIX century, with the invention of the bi-metallic electric thermostat in 1883, by Warren Johnson, for domestic heating systems, [1]. Since then, those devices have played an increasingly important role in society.

The word sensor comes from the Latin *sensus*, to feel. A sensor's main purpose is to detect an event or change in its environment (temperature, pressure, light intensity, etc.) by transforming it into a signal, usually electrical. To clarify this definition, a bi-metallic strip will be taken as an example, see Figure 1-1 below. This device consists of two metal bands connected to an electronic circuit; the bands are made of different materials, so that one expands more with thermal variation than the other; when the temperature of the ambient increases ( $\Delta T$ ), the strip curls closing the loop. In other words, it detects a change in temperature by altering its shape, thus letting current flow in the system [2].

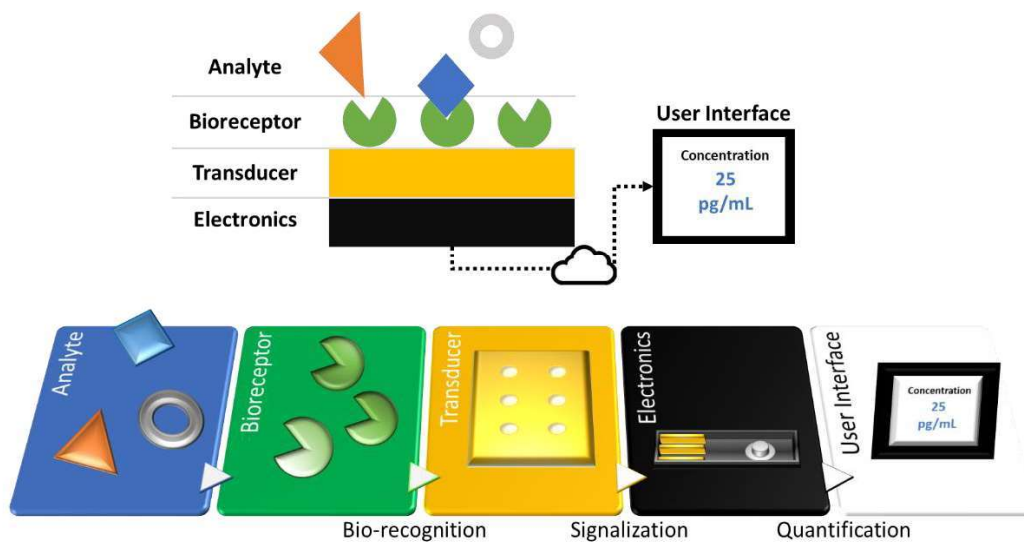


The constant technological development made sensors smaller, cheaper, and wide their applications. Robots, self-driven cars, smart-house and the Internet of Things (IoT), to name only a few, are a reality today due to sensing developments [3]. Among these wide range of uses, biosensing stands out as a blossoming research area. Biosensing is a multidisciplinary field of science and technology that involves physics, chemistry, biology, engineering and medicine. Aiming at improving the quality of life, it is now ubiquitous in biomedical diagnosis [4], drug development [5], food control [6], and many others. The database of the Web of Sciences indexes almost 13,000 reports on this topic from 2015-2020 [7].



According to Estrela et.al.[8], biosensors are devices capable of detecting biological or chemical reactions of generating signals dependent on the interaction between reagents. They are typically composed of the following components, as displayed in Figure 1-2: analyte: substances that are to be detected; bioreceptor: a molecule or biological entity that reacts with the analyte, producing a bio-recognition; transducer: any element which converts one form of energy into another; electronics: the circuitry that processes the output of the transducer in a readable data; and lastly, a user interface where the operator can access the results of the analysis [8], in a IoT scenario this display can be any interface where the user can access the data.

**Figure 1-2** – Schematic of a biosensor. Analyte, Bioreceptor, Electronics, and User Interface.



The first biosensor dates back to 1956 when Clark developed the oxygen electrode; a system designed to detect the levels of oxygen ( $O_2$ ) in blood, water, and other liquids [9]. The device uses a Teflon membrane as bioreceptor for the analyte ( $O_2$ ): when the molecules are sensed, the bio-recognition produces a charge variation that is read by an electronic circuit. Even though ionic charge was firstly used as signaling, it was the advent of photonics that enabled the revolutions to come, as Vo-Dinh states in his “Biomedical Photonics – Handbook”[10].

The use of photonics in biosensing started in 1980’s with the first Surface Plasmon Resonance (SPR) and fiber-optics based sensors [11]. The operation of these systems will be detailed in the following sections. For now, it is important to give an idea of the remarkable sensitivities achieved by these sensors. Sensitivity can be defined as the minimum concentration of analyte a biosensor can resolve [8]. In 1983, Leimberg experimentally

reported the first SPR sensor capable of detecting the presence of antibodies in aqueous solution with a concentration of 2  $\mu\text{g/ml}$  [11]; this is equivalent to detect a single grain of sugar in one liter of water. At the present time, some groups report the detection, using plasmonics, of concentrations in the order of  $\text{pg/ml}$  [12]–[14], which is equivalent to a single grain of sugar in a lake, of the size of 10 Olympic swimming pools.

Optical-based biosensors have brought noteworthy advances in biomedical analysis, thus facilitating the diagnosis and prognosis of diseases [4]. However, these devices are not yet found in a simple integrated form, like a pregnancy test, for example. They typically require complex equipment, usually employed in clinical facilities and with trained personnel, which make them expensive [4], [8]. Therefore, there is an urging need for technologies to make these systems smaller, cheaper, and easier to operate.

It is in this scenario that arises the concept of Point-of-Care (POC) devices. POC's are devices that allow the analysis of a biological sample in an affordable, fast, reliable, and user-friendly way [4], [15]. An example of a POC is the blood sugar monitor commonly found in drugstores. Business analysts estimate that by 2022 the biosensor's market will be worth over 25 billion dollars [16].

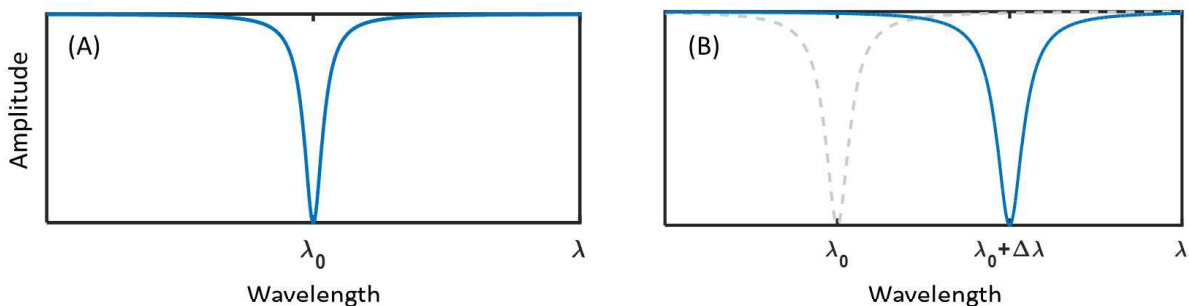
These challenges, together with growing investments in the field, make this a promising area of research towards the so-called lab-on-a-chip (LoC): an equipment that would incorporate all laboratory functions into a single chip [17]. One of the main drivers for these technologies is the detection of diseases in resource-limited countries [18]. Cost-effective, optical-based biosensors are the building blocks for the achievement of LoC, due to its miniaturization, low energy consumption, among other features. In this context, the field of photonics plays a crucial role.

## 1.2 Photonics in biosensing

Photonics is the field of science that studies the interaction of light with matter, specially under conditions where its particle aspect – the so-called photon –, is relevant; just as electronics aims at harnessing electrons, photonics aims at doing the same with photons [19]. Lasers, light emitting diodes (LEDs), optical-fibers, photonic-computers, and quantum-electronics are some of the technological advances brought by photonics [20]. As the XX century was revolutionized by advances in electronics, the same revolution is expected with photonics in the XXI century.

In the biosensing scenario, photonics has been successfully employed by several means [21]. The manipulation of light's properties (amplitude, phase, frequency, polarization, etc.) is used in techniques such as, refractometry [22], fluorescence[20], and light absorption[23]. Most of these photonic biosensing techniques rely on the detection of variations in the refractive index (RI) of a sample [21], essentially caused by the presence of an analyte.

Figure 1-3 – Spectrum change due to refractive index variation

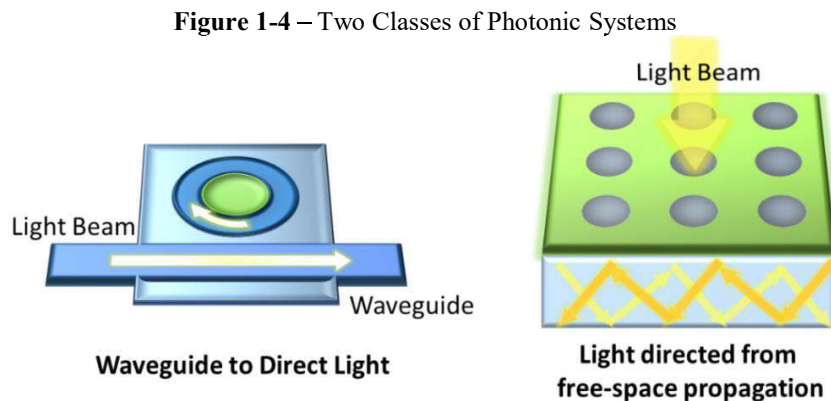


For the sake of illustration, suppose that a biosensor's transducer, without the analyte, has a response to a light source as shown in the Figure 1-3(A). This response typically represents a sample's transmittance or reflectance. The physical origin of such plot line will be discussed in more details in the section 2.4; for now, it is important to notice that this is a typical resonant behavior, where the spectrum is characterized by a dip in the amplitude at the wavelength  $\lambda_0$ , so that  $\lambda_0$  is termed the "resonant wavelength". Unsurprisingly, this resonant behavior is very dependent on the RI of the medium. When the analyte is detected, the variation in the RI of the sample changes the resonance wavelength, thus shifting the dip to the point  $\lambda_0 + \Delta\lambda$ , as shown in Figure 1-3(B). The dependence of the resonant wavelength on the refractive index, therefore, is the essence of the interrogation mechanism [15]. Photonic

biosensors relying on this kind of resonant response are one of the most important classes of sensors [15], [24], [25] and they are the main focus of this dissertation.

These sensors are typically characterized by their bulk sensitivity ( $S_B$ ) and Q-Factor.  $S_B$  is defined as the ratio between the wavelength shift ( $\Delta\lambda$ ) and the refractive index change ( $\Delta n$ ) and has units of nm/RIU [15], where RIU stands for Refractive Index Units. As will be explained in more details in section 2.5, the bulk term is related to a change in the RI in the entire medium where the analyte is present. The Q-Factor, on the other hand, is a dimensionless figure-of-merit that expresses the resonance's sharpness. The physical origin and proper interpretation of this parameter will also be presented in 2.5. Another figure-of-merit commonly used to define the precision of a transducer biosensor is the limit-of-detection (LOD). Essentially, the LOD expresses the minimum change in the RI that the system can resolve, typically given in RIU; for instance, if a sensor has a LOD of  $10^{-6}$  RIU, it is able to detect changes up to a millionth in the refractive index of the medium.

Photonic biosensors can be found in a variety of architectures [20]. However, they can be divided into two broad classes, according to the medium used to direct light into the sensor: in one class a waveguide is required, whereas in the other class light is directed by free-space propagation. Figure 1-4 illustrates these two approaches. Typically, waveguide-required devices boast of higher sensitivity, but at the expense of complexity, mainly due to the requirement of coupling light into the waveguide [24], [26]. Examples of waveguide-based sensors are: planar, slot, and photonic crystals (PhC) waveguides [24], fiber-optics sensors [23], SPRs [27]; and the microcavity resonators, like, ring-resonators [26] and photonic crystal cavities [28]. A summary of these systems is shown in Table 1. Examples of more exotic systems can be found in [15].



Photonic biosensors that do not require waveguide coupling, on the other hand, exhibit many operational advantages – like facile integration and real time, label-free detection [29].

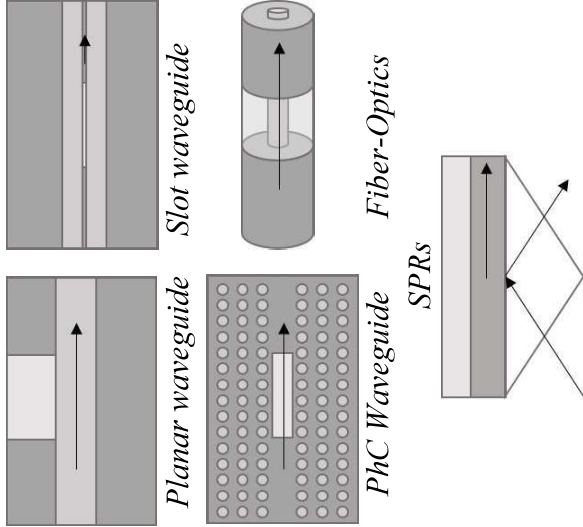
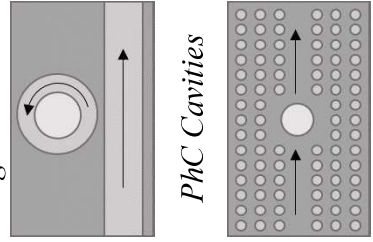
Their downside is their lower sensitivity when compared with waveguide-based sensors. These features make these devices promising options for Point-of-Care and Lab-on-a-Chip applications [4]. Examples of such devices are the Localized Surface Plasmons Resonances (LSPR) [30] and the Quasi-Guided modes (or, as is more commonly found in the literature, Guided Mode Resonance GMR) sensors [31].

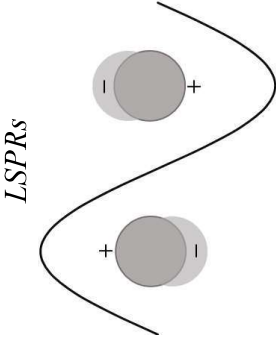
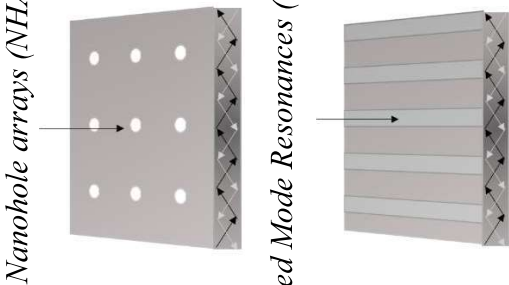
The operation of LSPR sensors is based on the interaction of light with metallic nanoparticles [32]. These particles are typically smaller than the wavelength of light, causing this interaction to be strongly dependent on their shapes and sizes [33]. Spheres, rods, stars, and prisms are some of the nanostructures geometries that have been successfully employed in biosensing applications [25]. Even though much progress has been obtained in the last years, there are still challenges to overcome such as the improvement of the limit-of-detection and selectivity of these systems [34]. The physical concepts and working mechanism of these sensors will be explained in the section 2.1.

Another type of free-space sensors are the devices based on excitation of quasi-Guided modes (QGM). QGM-based sensors feature as one of the most promising photonic systems for biosensing applications mainly due to their cost-effective fabrication process, easy integration on chip, and capacity to control the wavelength of operation by design [24], [29], [31]. QGM sensors uses periodic structures, such as gratings and nanoarrays, to couple light into a waveguide. The details of the physical operation behind this type of sensor will be detailed in section 2.3. They can be implemented in both dielectric [35], [36] and metallic (plasmonic) [14], [37] waveguides. Although some progress has been made in trying to unify these two worlds [38], [39], most of the current research focuses on only one of these types.

In general, metallic-based, or plasmonic, QGMs display high sensitivity at the expense of a poor spectrum, with low amplitudes and broad resonances, the reason why this occurs is explained on 2.2.2. For instance, Li et. al. were able to sense single cells secretion [37], [40], Kilic et. al. achieved drug screening [41], and Soler et. al. performed simultaneous detection of two distinct analytes [42] by using biosensor design based on surface plasmon propagation, capable of sensing changes in the order of  $2 \times 10^{-5}$  RIU, with sensitivity of 671 nm/RIU, though with a maximum transmitted amplitude of less than 10% of the emitting source and a Q-Factor of only 30 [39]. This sensor consisted in a thin layer of gold patterned with an array of nanoholes over a glass substrate. A similar design was used by Monteiro et. al. achieving astonishing theoretical sensitivities as high as 4,000 nm/RIU [43], [44]. Gomez-Cruz et. al, using a similar approach, with silicon nitrate as a substrate instead of glass, were able to detect bacteria activities [45], displaying resolution up to  $10^{-6}$  in the refractive index change.

**Table 1** – Waveguide-based photonic biosensors technologies

	<b>Working Mechanism</b>	<b>Pros and Cons</b>	<b>Typical Sensitivities</b>
 <p><i>Planar waveguide</i></p> <p><i>Slot waveguide</i></p> <p><i>PhC Waveguide</i></p> <p><i>Fiber-Optics SPRs</i></p>	<p>These systems operation is based on detecting changes in the evanescent part of the waveguide mode.</p> <p>They usually interrogate resonance shifts in the transmission or reflection spectra.</p>	<p>☺</p> <ul style="list-style-type: none"> <li>• High sensitivities,</li> <li>• Low cost of fabrication;</li> </ul> <p>☹</p> <ul style="list-style-type: none"> <li>• Sensitive to thermal variations;</li> <li>• Complex integration due to light coupling needs;</li> </ul> <p>[15]</p>	<p><i>Planar Waveguide</i></p> <p>D: 200 nm/RIU [46]</p> <p><i>Slot Waveguide</i></p> <p>D: 400 nm/RIU [24]</p> <p><i>Fiber Optics</i></p> <p>D: 60 nm/RIU[47]</p> <p><i>SPRs</i></p> <p>M: 10<sup>4</sup> nm/RIU [48]</p>
 <p><i>Ring Resonators</i></p> <p><i>PhC Cavities</i></p>	<p>These systems operation is based on the integration between the cavity and the waveguide. In a cavity or resonator, the light is trapped and has a very sharp and well-defined resonance.</p>	<p>☺</p> <ul style="list-style-type: none"> <li>• The most sensitive systems; LOD down to 10<sup>-8</sup> RIU;</li> </ul> <p>☹</p> <ul style="list-style-type: none"> <li>• Intolerant to fabrication imperfections;</li> <li>• Complex integration due to light coupling needs; [49]</li> </ul>	<p><i>Ring Resonator</i></p> <p>D: 300 nm/RIU [26]</p> <p>M: 1000 nm/RIU[50]</p> <p><i>PhC Cavities</i></p> <p>D: 1500 nm/RIU [28]</p>

	<b>Working Mechanism</b>	<b>Pros and Cons</b>	<b>Typical Sensitivity</b>
 <p><i>LSPRs</i></p>	<p>These systems work based on interaction of light and metallic nanoparticles.</p> <p>Can interrogate in resonance change, light absorption and fluorescence.</p>	<p>☺</p> <ul style="list-style-type: none"> <li>• Low fabrication cost;</li> <li>• Easy integration;</li> </ul> <p>☹</p> <ul style="list-style-type: none"> <li>• Limited level of detection;</li> <li>• The bigger the particle more assays it can detected, however, the lower is the sensitivity [34]</li> </ul>	<p>100 nm/RIU[32]</p>
 <p><i>Nanohole arrays (NHA)</i></p> <p><i>Guided Mode Resonances (GMRs)</i></p>	<p>These system uses periodic structures, such as gratings and nanoarray, to couple light in the system. They work based on quasi-guided mode detecting changes in the evanescent light.</p>	<p>☺</p> <ul style="list-style-type: none"> <li>• Low cost and easy fabrication</li> <li>• Direct Light coupling</li> <li>• Best approach for LoC devices</li> </ul> <p>☹</p> <ul style="list-style-type: none"> <li>• Lower Sensitivities; [31]</li> </ul>	<p><i>GMR</i></p> <p>D: 100 nm/RIU [24]</p> <p><i>NHA</i></p> <p>D: 300 nm/RIU [36]  M: 600 nm/RIU[40]</p>

Dielectric-based sensors, on the other hand, typically demonstrate complementary properties when compared to their plasmonic counterpart. Indeed, dielectric-based sensors typically show sharp resonances but with lower sensitivities. Wang et. al. reported a sensitivity of 300 nm/RIU with a Q over 5000, using a silicon-on-insulator (SOI) photonic biosensor patterned with a nanohole array [36]. In another paper, the same group reported a theoretical sensitivity over 800 nm/RIU with a Q at the scale  $10^7$ , operating in the telecom range, by using a double slab of SOI[51]. The experimentally measured sensitivity, however, is only 100 nm/RIU [52]. Lin et. al. reported a Guided Mode Resonance (GMR) based sensor able to detect concentrations of 75 ng/mL [53] and Triggs et. al., via chirped GMR achieved 150 nm/RIU, able to detect concentrations down to 40 ng/mL[35]. A summary of QGM systems is shown in Table 2.

### **1.3 Objective and Text structure**

Even though some papers discuss characteristics of both plasmonic and dielectric systems [24], [36], [49], [54], it is usually difficult to find in the literature a standardized approach which discriminates the main features of these devices, because each group tends to use a different platform, thus hindering a comparative assessment of the devices. Consequently, given their complementary aspects and mostly independent research effort, it is still an open question which kind of sensor, dielectric or plasmonic based, has the best overall performance. In this scenario, there is a need for a systematic comparison between these two QGMs sensors. This dissertation aims at accomplishing this task by systematically studying and comparing the core differences between both systems in terms of their sensing performance and spectral characteristics. The present work is divided into four chapters: 1 - Introduction; 2 - Physical Concepts, where the physics involved in the mentioned systems is presented; 3 - Dielectric versus Metallic based media Sensors, where it is shown and discussed the results obtained in the preliminary simulations; 4 - Dielectric Biosensor based on a-Si, where the author propose a new biosensor design based on amorphous Silicon; and, finally, 5 - Conclusions.



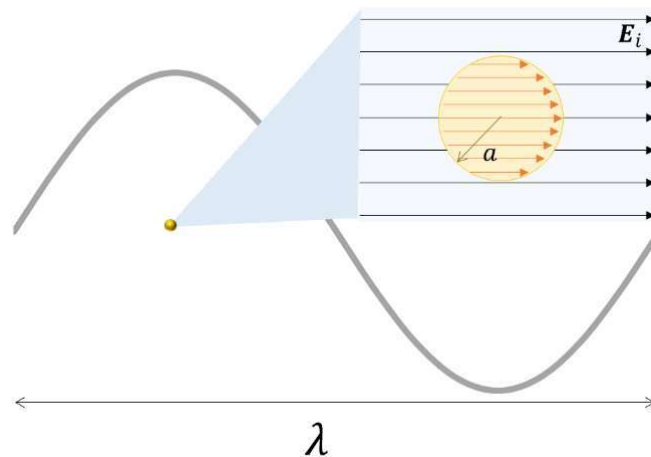
## 2 PHYSICAL CONCEPTS

As stated in the previous section, biosensors can be found in a variety of forms and configurations. The goal of the current section is to present the physical phenomena behind the most employed biosensing systems and to understand their working mechanism. Here it will be described the characteristics of localized, guided, and quasi-guided modes.

### 2.1 Localized modes

The nature of a localized surface plasmon resonance (LSPR) is intimately related to the concept of scattering – the random spread of a light front caused by the interaction with a small particle. This phenomenon can be classified into two regimes, depending on the size of the object: when it is many times smaller than the wavelength of light ( $\lambda$ ) which it interacts, the physical behavior is described by Rayleigh scattering; if the particle size is in the order of  $\lambda$ , then, Mie scattering shall be used. The main difference between these two theories is associated with the propagation of the harmonic field inside the particle: in Rayleigh's scattering, the phase accumulation by the wave propagating inside the particle is negligible, thus justifying a quasi-static approximation – as shown in Figure 2-1; in Mie's scattering, the phase accumulation is no longer negligible, requiring the use of the full set of Maxwell's equations. For this section, which focus on the understanding of the LSPRs behavior, Rayleigh's scattering will be outlined in more details.

Figure 2-1 – Quasi-static approximation

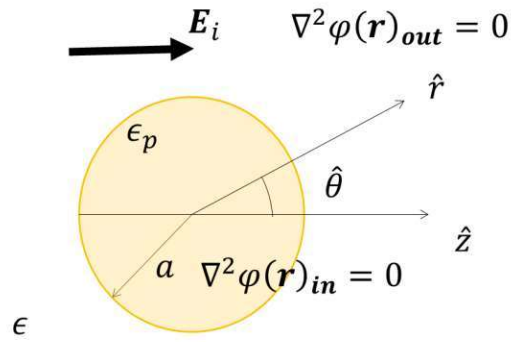


As illustrated in Figure 2-1, because the wavelength inside the material ( $\lambda$ ) is much larger than the particle radius  $a$  ( $\lambda \gg a$ ) the phase of the harmonically oscillating electromagnetic field is virtually constant over the particle volume, so that one can calculate the spatial field distribution by assuming the simplified problem of a particle in an electrostatic field, which is fully described by the Laplacian equation

$$\nabla^2 \varphi(\mathbf{r}) = 0 \quad (2.1.1)$$

where  $\varphi(\mathbf{r})$  is the electrostatic potential. The only remaining challenge is to solve equation 2.1.1 for both inner and outer the sphere: assuming spherical coordinate system with the origin at the center of the sphere – shown in Figure 2-2, where  $\mathbf{E}_i$  is the incident field, for this example  $\mathbf{E}_i = E_i \hat{\mathbf{z}}$ ,  $\epsilon$  is the dielectric constant of the homogenous surrounding medium and  $\epsilon_p$  is the dielectric constant of the particle. Applying the proper boundary conditions, leads to equations 2.1.2 [55]:

**Figure 2-2** – Small sphere in a uniform electric field



- I. The symmetry in relation to  $\hat{\theta}$  implies that:

$$\varphi(\mathbf{r} = a)_{out} = \varphi(\mathbf{r} = a)_{in} \quad (2.1.2a)$$

- II. The continuity of the normal components of the displacement field implies that:

$$\begin{aligned} \epsilon \mathbf{E}(\mathbf{r} = a)_{out} &= \epsilon_p \mathbf{E}(\mathbf{r} = a)_{in} \\ \epsilon \frac{\partial}{\partial \mathbf{r}} \varphi(\mathbf{r} = a)_{out} &= \epsilon_p \frac{\partial}{\partial \mathbf{r}} \varphi(\mathbf{r} = a)_{in} \end{aligned} \quad (2.1.2b)$$

- III. At a great distance from the particle, the total field will be the incident:

$$\lim_{r \rightarrow \infty} \varphi(\mathbf{r})_{out} = -\mathbf{E}_i \mathbf{z} \quad (2.1.2c)$$

Putting all these conditions together will lead to the solution for this problem (2.1.3), and more details can be found in Chapter 5 of Maier's Plasmonics: Fundamentals and Applications [56] equations 5.5.

The solution to the potential is:

$$\varphi(\mathbf{r})_{in} = -\frac{3\epsilon}{\epsilon_p + 2\epsilon} r \cos(\theta) \mathbf{E}_i \quad (2.1.3a)$$

$$\varphi(\mathbf{r})_{out} = -r \cos(\theta) \mathbf{E}_i + \frac{\epsilon_p - \epsilon}{\epsilon_p + 2\epsilon} \frac{a^3}{r^2} \cos(\theta) \mathbf{E}_i \quad (2.1.3b)$$

Now, taking the divergent of electrostatic potential ( $\varphi(\mathbf{r})$ ), in equations 2.1.3, will lead to the Electric Field inside and outside the sphere (since,  $\mathbf{E} = -\nabla\varphi$ ):

$$\mathbf{E}(\mathbf{r})_{in} = \frac{3\epsilon}{\epsilon_p + 2\epsilon} \mathbf{E}_i \quad (2.1.4)$$

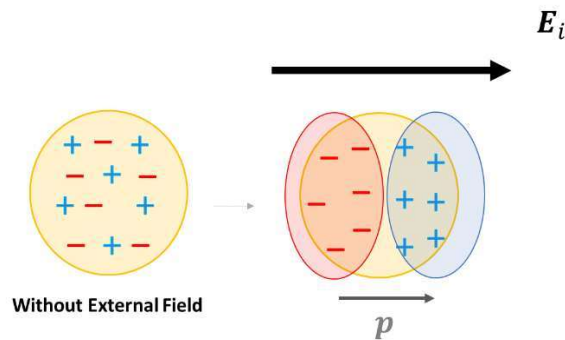
$$\mathbf{E}(\mathbf{r})_{out} = \mathbf{E}_i + \frac{3 \mathbf{n}(\mathbf{n} \cdot \mathbf{p}) - \mathbf{p}}{4\pi\epsilon_0\epsilon} \frac{1}{r^3} \cos(\theta) \quad (2.1.5)$$

Where  $\mathbf{n}$  is the direction normal to the sphere and  $\mathbf{p}$  is the dipole moment:

$$\mathbf{p} = 4\pi a^3 \epsilon_0 \epsilon \frac{\epsilon_p - \epsilon}{\epsilon_p + 2\epsilon} \mathbf{E}_i \quad (2.1.6)$$

For the inner field, the solution is proportional to incident field, whereas, the outer field solution is expressed in terms of the induced dipole moment ( $\mathbf{p}$ ) (2.1.5). Important intuition on the physics of Rayleigh scattering is gained by this description: the presence of the incident field inside the particle causes an oscillation on its charges (the bonding between the material molecules will dictate how severe will be this movement), thus inducing the dipole moment ( $\mathbf{p}$ ), as illustrated in Figure 2-3.

Figure 2-3 – Dipole moment induced from an external field

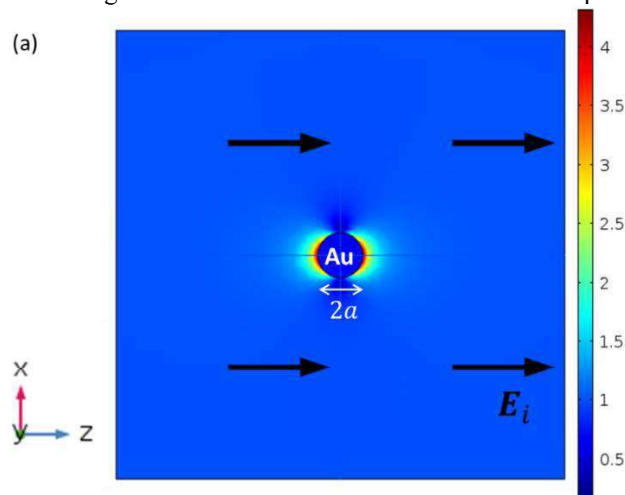


In essence, equation 2.1.5 implies that the scattered field can be interpreted as being the superposition of the applied field ( $\mathbf{E}_i$ ) and the field emitted by the induced dipole ( $\mathbf{p}$ ), which is located at the center of the particle. Also, taking a closer look at 2.1.6, it is noticeable that the strength of  $\mathbf{p}$  is proportional to the sphere's volume and the relation  $\frac{\epsilon_p - \epsilon}{\epsilon_p + 2\epsilon}$ . Even though this relation is valid for spheres of any material, it is particularly interesting when applied to metallic ones. According to Drude's model [57], metals display complex dielectric constants, with the real part being negative. Therefore, at a certain value, accurately,  $Re[\epsilon_p] = -2\epsilon$ , equation 2.1.6 reaches a resonant behavior (associated to a maximum of the equation). Also notice that the denominator is never "0" due to the imaginary part of the dielectric constant. When the real parts of the denominator in equation 2.1.6 cancel each other, the scattering is maximized, which is the signature of the excitation of a LSPR.

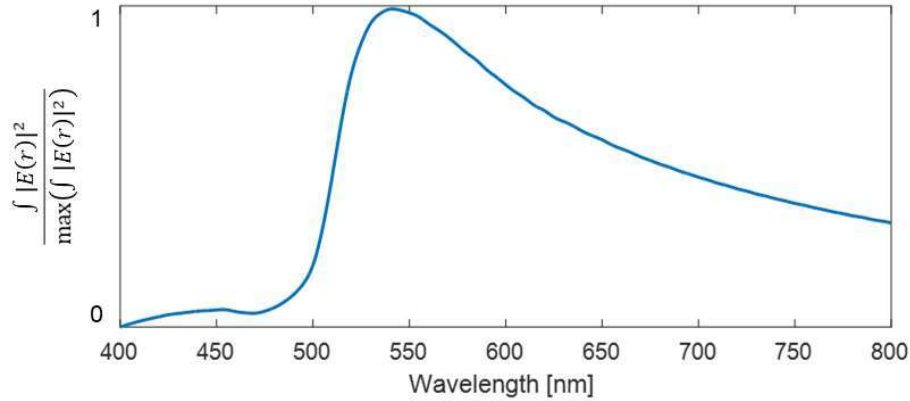
The resonant behavior can be straightforwardly described as resulting from the attraction of the electrons in the interface dielectric/metal caused by the incident electric field; these electrons are weakly coupled with their nuclei in metals – considered as an electron-cloud – and the curved surface of the particle exerts an effective restoring force on them, thus leading to a system analogous to a harmonic oscillator. The resonant frequency, therefore, depends on the restoring force, which enters the macroscopic equations through the dielectric constant. On resonance, there is a strong field amplification in the near-field zone outside the particle: notice that the LSPR mode is strongly localized near the sphere, as shown in Figure 2-4. It is this strong field localization that makes LSPR interesting for sensing applications.

**Figure 2-4** – Simulation of a LSPR mode on resonance

Gold nanosphere with radius ( $a$ ) of 10 nm illuminated by a plane wave with wavelength of 550 nm. It is noticeable that there is a strong field enhancement in the vicinity of the sphere. The plot displays the norm of the Electric Field, the reddish regions are maximum values and the blueish represent the minima.



b) Near field dependence on the wavelength, showing a broad resonance with a peak at 550 nm.



It is important to notice that equations 2.1.3 – 2.1.6 are only valid for a quasi-static regime, where  $a \ll \lambda$ ; on the other hand, when the size of the particle is of the order of the wavelength, it is necessary to apply the boundary conditions for the full set of Maxwell's equation, which amounts to Mie's Theory. The mathematical derivation of this model can be found in details in the chapter 4 of Bohren and Huffman's Absorption and Scattering of light [55]. Furthermore, the use of the quasi-static approximation implies that the resonance of the LSPR mode does not depend on the particle's size<sup>1</sup>, just on the material permittivity  $\epsilon_p$ , meaning that once  $\epsilon_p$  is known the resonance frequency is determined. In Mie's theory this conclusion is no longer valid, and the resonance is also dependent on the object's size and shape.

In the context of sensing, the main advantage of LSPR is that they can be directly excited by free space propagation. Such modes, however, feature very broad resonances (see Figure 2-4b), which is detrimental to their applications on sensors. Guided modes, on the other hand, feature much sharper resonances and are the subject of the next section.

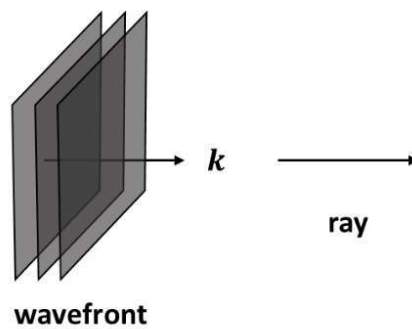
---

<sup>1</sup> The dipole moment strength does depend on the particle radius as defined on 2.1.6, however the resonance does not, since it is the relation  $\frac{\epsilon_p - \epsilon}{\epsilon_p + 2\epsilon}$  that determines it.

## 2.2 Guided modes

Differently from localized modes, the electromagnetic field of a guided mode spans the entire waveguide. The main goal of the present section is to lay out the basic concepts of waveguide theory. For this purpose, the ray optics approach is very useful and insightful. In the rays optics picture the plane wave propagation direction, determined by the wavevector ( $\mathbf{k}$ ), is represented by a ray pointing in the same direction of  $\mathbf{k}$  - Figure 2-5 [58].

**Figure 2-5** – Ray optics description  
 $\mathbf{k}$  is the wavevector and dictates the pointing direction of the ray



Consider first the Snell's Law. This simple equation (2.2.1) comes directly from the application of the boundary conditions[59] or, more generally, from translation symmetry, that imposes the conservation of the parallel wave vector component[60]

$$\theta_i = \theta_r \quad (2.2.1a)$$

$$n_i \sin(\theta_i) = n_t \sin(\theta_t) \quad (2.2.1b)$$

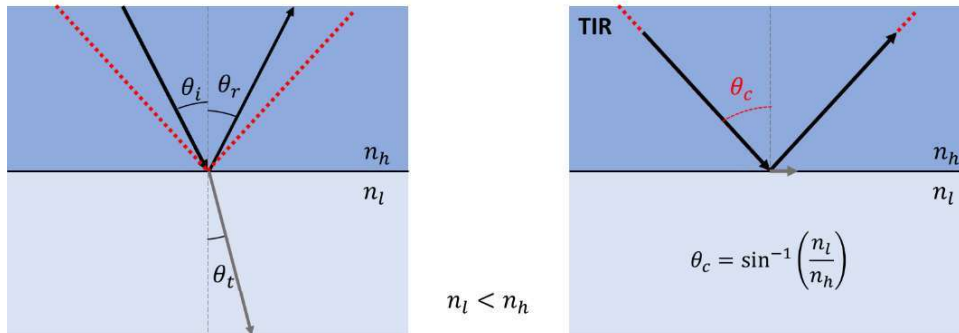
where  $n_i$  is the refractive index (RI) of the medium of incidence,  $n_t$  is the RI of the medium of transmission,  $\theta_i$  is the incident angle and  $\theta_t$  is angle of transmission (or, equivalently, the angle of refraction). Notice that when a wave light coming from a higher index medium is incident on a lower index medium ( $n_i > n_t$ ), there can be an incident angle above which no light is transmitted: this condition is called total internal reflection (TIR) and this angle is named critical angle ( $\theta_c$ ), as illustrated in Figure 2-6. TIR cannot be met if the light is coming from a lower index medium ( $n_i < n_t$ ). Moreover, the phase shift associated with reflection comes directly from the Fresnel coefficients, and it is dependent on the light polarization [58].

Another manner of understanding this process is via the Goos-Hanchen Shift (GHS). GHS, in general, refers to the lateral shift along the interface when a light beam experiences total internal reflection. The GHS, which can be found on Example 7.5.7 of Orfanidis

Electromagnetic Waves and Antenna [57], leads to the same mathematical conclusion of the phase shift described by Fresnel Equations.

**Figure 2-6** – Total internal reflection.

Left side: incident angle lower than the critical angle. Right: incident angle higher than the critical angle.

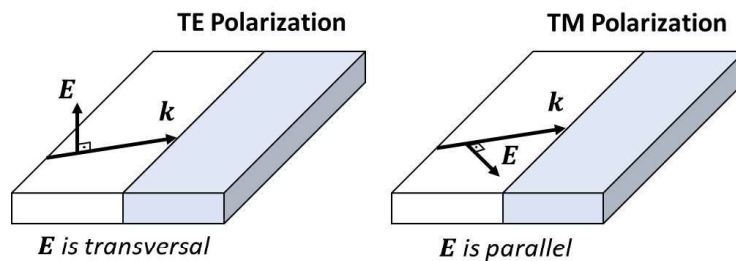


Before proceeding, it is important to remark the two most significant polarizations, illustrated in Figure 2-7: The Transverse Electric (TE) polarization where the Electric field is transverse to the incidence plane, also termed *s* polarization (*s* for *senkrecht*, perpendicular in German), and the Transverse Magnetic (TM) polarization where the Magnetic Field is perpendicular – or the Electric Field is parallel – to the incidence plane, sometimes referred as *p* polarization (*p* for parallel Electric Field). For angles of incidence larger than the critical angles, the phase shifts are given by:

$$\phi_{TE} = 2 \tan^{-1} \left[ \frac{\sqrt{\sin^2(\theta_i) - \sin^2(\theta_c)}}{\cos(\theta_i)} \right] \quad (2.2.2a)$$

$$\phi_{TM} = 2 \tan^{-1} \left[ \frac{\sqrt{\sin^2(\theta_i) - \sin^2(\theta_c)}}{\cos(\theta_i) \sin^2(\theta_c)} \right] \quad (2.2.2b)$$

**Figure 2-7** – TE and TM Polarizations,

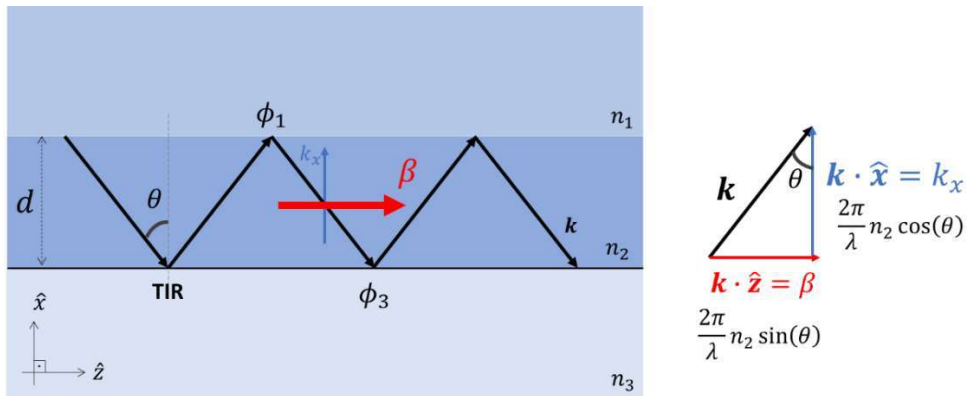


### 2.2.1 Slab waveguide

Now, consider not just one interface, but two, thus constituting what is called a “slab waveguide”, shown in Figure 2-8, where  $n_2 > n_3 \geq n_1$  and  $d$  is the thickness of the slab with higher index, which is denoted the waveguide’s core. If there is a ray propagating in the central medium ( $n_2$ ), when the TIR condition is satisfied at both interfaces, the light will be confined in  $n_2$ . However, just the trapping of the ray does not satisfy the guiding process; the light wave must also interfere constructively with itself inside the guiding medium [58], [59], [61]. This state is achieved when the phase difference of two consecutive wave-fronts is a multiple of  $2\pi$ . In other words, the round trip of a ray is a multiple of  $2\pi$ . This condition is typically called self-consistence of the wave, also transverse resonance. Therefore, only a certain discrete number of incidence angles will satisfy it. The field distribution associated with rays propagating at angles that assure the self-consistence criterion is called a waveguide mode[58].

**Figure 2-8 – Slab Waveguide**

$n_1, n_2,$  and  $n_3$  are the refractive indexes of the media.  $k_x$  and  $\beta$  are the  $x$  and  $z$  components of the wavevector, respectively,  $\lambda$  is the free space wavelength,  $n_{eff}$  is effective index of the waveguide,  $\theta$  is the incident angle, and  $\phi_1$  and  $\phi_3$  are the phase shift imposed in by the TIR on the interfaces.



One important characteristic of the waveguide mode is its propagation constant ( $\beta$ ). In essence, it tells the phase velocity of the wave in the direction of propagation (see Figure 2-8). The propagation directions allowed in this guide – Figure 2-8 – are parallel to the  $\hat{z} - \hat{y}$  plane, but for convenience the ray will be considered to propagate in  $\hat{z}$ . In this case,  $\beta$  is the  $\hat{z}$  component of the wavevector in the medium, equation 2.2.3, where  $\theta$  is the incidence angle.

$$\beta = \mathbf{k} \cdot \hat{\mathbf{z}} = \frac{2\pi}{\lambda} n_2 \sin(\theta) \hat{\mathbf{z}} \quad (2.2.3)$$



The self-consistence condition is described mathematically by the phase accumulated in the  $x$  direction within one round-trip of the wave, which determines the allowed angles  $\theta$  and, consequently,  $\beta$ . Explicitly, the round-trip phase accumulation is:

$$2 \left( \frac{2\pi}{\lambda} n_2 \cos(\theta) \right) d - \phi_1 - \phi_3 = m2\pi \quad (2.2.4)$$

Where  $\mathbf{k}_x = \frac{2\pi}{\lambda} n_2 \cos(\theta)$  is the  $x$  component of the wavevector,  $d$  is the thickness of the waveguide's core,  $\lambda$  is the free-space wavelength,  $\phi_1$  and  $\phi_3$  are the phase shift imposed by the total internal reflection on the upper and lower boundaries, since the expressions for TM and TE are negative they appear subtracting in 2.2.4, respectively, and  $m$  is an integer. The only unknown in 2.2.4 is  $\theta$ , because once the polarization is established the  $\phi$ 's are determined by the Fresnel coefficients. For TE polarization, for instance, assuming a symmetric guide, where  $n_1 = n_3$ , and using the  $\phi_{TE}$  equation 2.2.2a,  $\theta$  could be found via:

$$\tan \left( \pi \frac{d}{\lambda} n_2 \cos(\theta) - m \frac{\pi}{2} \right) = \sqrt{\frac{\sin^2(\theta_c)}{\sin(\theta)} - 1} \quad (2.2.5)$$

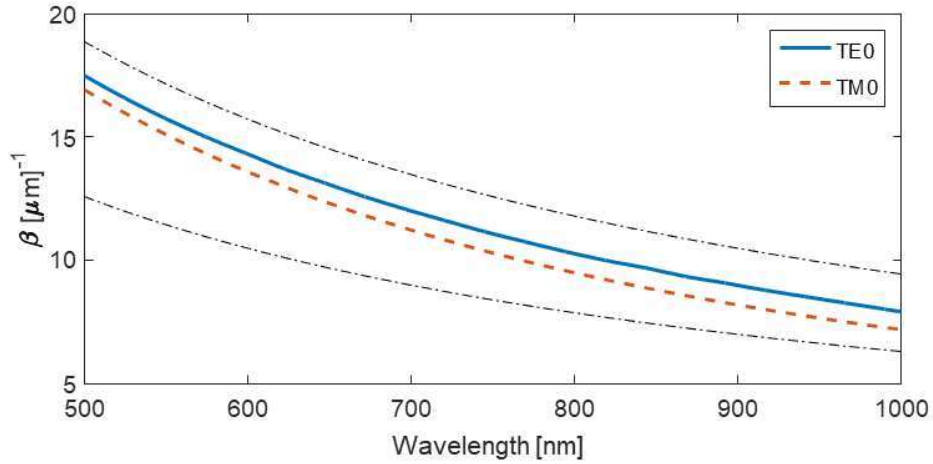
Equation 2.2.5 does not have an analytical solution, and it is called the transcendental equation of the waveguide, for TE polarization[58]. The same process can be used to derive the transcendental equation of TM polarization, just using  $\phi_{TM}$  instead of  $\phi_{TE}$  in 2.2.4. Every  $m$  will determine  $\theta_m$ , which is associated with a mode in the waveguide, thus defining a specific  $\beta_m$ . The modes' phase velocity can also be expressed through the effective refractive index ( $n_{eff}$ ), defined as in Equation 2.2.6, where  $k_0$  is the free-space wavevector and  $n_1 = n_3 < n_{eff} < n_2$ .

$$n_{eff} = \frac{\beta_m}{k_0} \quad (2.2.6)$$

A plot of the propagation constant against the wavelength (or frequency) is typically called the “dispersion diagram”, as the one shown in Figure 2-9. More on waveguides can be found in [62]. The dispersion plays an important role in photonic biosensors, as will be discussed in the next section.

**Figure 2-9 – Waveguide dispersion**

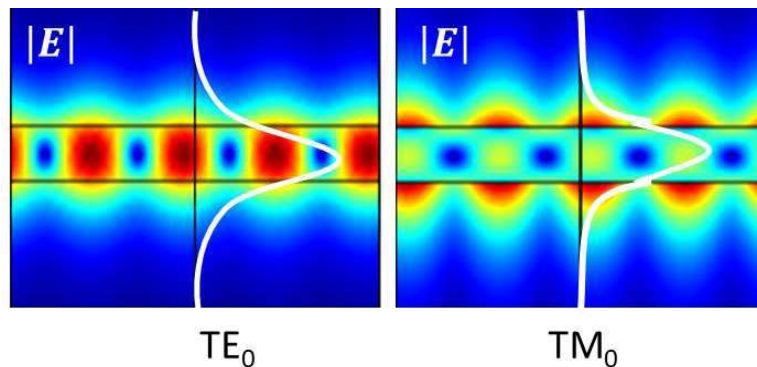
Solid line represents the TE fundamental mode and the dashed line the TM one, the black dashed point lines are the light line in the cover (lower limit) and in the core (upper limit), demonstrating that all guided-modes satisfy  $n_1 k_0 < \beta < n_2 k_0$ . The structure simulated on MatLab consisted of a slab waveguide with thickness of 100 nm and refractive indexes:  $n_1 = n_3 = 1.0$  and  $n_2 = 1.5$ ; the wavelength span for 500 to 1000 nm.



Although the ray optics description is sufficient to find the waveguide dispersion, it cannot be used to calculate the electromagnetic field distribution inside the waveguide. In order to find the field profiles, it is necessary to use Maxwell's equations and apply the boundary conditions, with the requirement that the field oscillates in the vertical direction inside the waveguide, but that it decays exponentially outside the waveguide core [57], [61]. This exponential decay is usually referred to as the evanescent part of the mode, or evanescent field. One example of field distribution in a waveguide is displayed in Figure 2-10: it is evident that the field displays an oscillating characteristic in the waveguide core and an exponential decay in the outside regions.

**Figure 2-10 – Waveguide modes**

Plot of the Electric Field norm. TE mode on the left and TM mode on the right. Note that the E field is continuous on the TE mode but not in the TM, also that it is much less confined in the core for this mode. In white is displayed the field distribution. The structure simulated on COMSOL via Eigen Solver consisted of a slab waveguide with thickness 100 nm and indexes of  $n_1 = n_3 = 1.0$  and  $n_2 = 1.5$



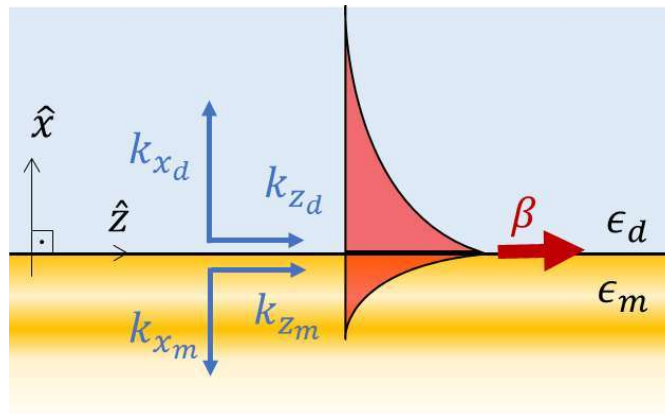
The evanescent part of a mode plays an important role in photonic biosensors. Evanescent field sensing can be applied to several different transduction approaches including evanescent fluorescence detection, monitoring of refractive index changes or detecting spectroscopic shifts[63]. Since the guided mode is strongly dependent on the constituting media, any change in the surrounding media optical properties perturb the modes, consequently making these structures great biosensor transducers.

### 2.2.2 Surface Modes

In the previous discussion, it was assumed that the slab waveguide consisted of a stack of dielectric materials; an interesting phenomenon, however, arises on the interface between a metallic and a dielectric slab. Consider an interface between a metal and an insulator (dielectric) – as shown in Figure 2-11, where  $\epsilon_m$  and  $\epsilon_d$  are, respectively, the metal and the insulator dielectric constants.

**Figure 2-11 – Surface Wave**

$\epsilon_d$  is permittivity of upper dielectric medium  $\epsilon_m$  for the lower metallic medium. This wave will display an evanescent profile at both sides and a propagating mode confined on the interface.  $\beta$  is the propagation constant of the mode, and the  $z$  component of the wavevector, and  $k_x$  is the  $x$  component of the wavevector.



At the interface between the two media, conservation of the parallel momentum ( $k_z$ ) and the boundary conditions of Maxwell's Equations ( $E_{zm} = E_{zd}$  and  $H_{ym} = H_{yd}$ ), lead to the relations expressed in equations 2.2.7 [56], where the subscript  $m$  refers to the metal part and  $d$  to the dielectric part,  $\mathbf{k}_z$  is the parallel component of the wavevector,  $\mathbf{k}_{xm}$  is the transversal component  $\mathbf{k}$ , and  $\epsilon$  is the dielectric constant. These solutions of Maxwell's equations refer to a special kind of propagating mode, which features an exponential decay at both sides, called a surface wave, shown in red in Figure 2-11.

$$\mathbf{k}_{zm} = \mathbf{k}_{zd} \quad (2.2.7a)$$

$$\frac{\mathbf{k}_{xm}}{\mathbf{k}_{xd}} = -\frac{\epsilon_m}{\epsilon_d} \quad (2.2.7b)$$

$$\mathbf{k}^2 = \mathbf{k}_z^2 + \mathbf{k}_x^2 \quad (2.2.7c)$$

This condition can only be achieved for TM polarization, because the Electric Field must have a component parallel to interface. As discussed in Section 2.1, according to Drude's Model [57], metals display complex permittivity with the real part being negative, for certain frequencies. Notice then, when  $Re[\epsilon_m] < 0$  and  $|\epsilon_m| > \epsilon_d$ ,  $\mathbf{k}_z$  will be real and  $\mathbf{k}_x$  will be purely imaginary, given rise to a mode that is confined at the interface between the two media. Defining the propagation constant  $\beta$  equal to  $\mathbf{k}_z$ , and arranging equations 2.2.7 – where  $\mathbf{k} \triangleq \mathbf{k}_0\sqrt{\epsilon}$ , one will get [56]:

$$\beta = k_0 \sqrt{\frac{\epsilon_d \epsilon_m}{\epsilon_m + \epsilon_d}} \quad (2.2.8)$$

The full derivation of the previous equations can be found in Chapter 2 of Maier's: Plasmonics Fundamentals and Applications[56]. Equation 2.2.8 is the dispersion relation of special type of mode called Surface Plasmon Resonance (SPR). SPR is the resonant oscillation of conduction electrons at the interface between negative (metal) and positive (dielectric) permittivity material stimulated by incident light [25].

The confinement of the SPR is ensured since the propagation constant  $\beta$  is greater than the wavevectors  $\mathbf{k}_d$  and  $\mathbf{k}_m$ , leading to evanescent decay on both sides of the interface. However, it implies that the mode cannot be directly coupled from the dielectric, requiring phase-matching techniques to do so. The most employed methods are prism, like Kretschmann configuration, and grating coupling (1D and 2D, in the form of nanoholes array) [56]. The latter will be explained in next section.

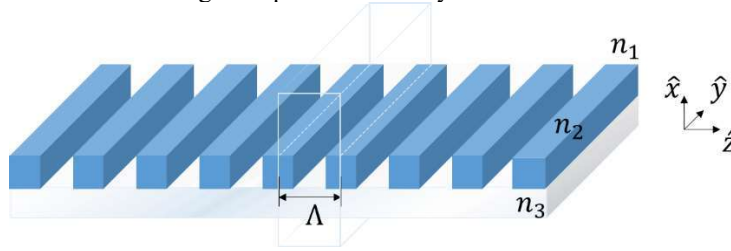
Surface Plasmon Resonance based sensors are widely used on biosensing platforms, mainly due to their strong dependence on the evanescent field [64]. In Section 3.1 a SPR sensor based on nanohole array is analysed in more details.

## 2.3 Quasi-guided modes

One of the main challenges in photonic biosensing is the integration of the transducer to the system. In this context, quasi-guided modes play an important role, due to their capability of coupling light directly from free-space. In this section, the basics of waveguide coupling will be outlined, starting with diffraction gratings.

**Figure 2-12 – Grating.**

$n_1, n_2$  and  $n_3$  are the refractive indexes of the constituting materials.  $\Lambda$  is periodic of the structure. The region marked region represent the unity cell of the structure.



A diffraction grating is made of two materials periodically arranged, as shown in the Figure 2-12. The symmetry arising from the periodicity imposes that the electromagnetic modes of the system are also periodic [60]. Figure 2-12 shows a grating infinite in the  $yz$  plane, and periodic on the  $\hat{z}$  direction. Therefore, the wavevector components in this direction will display the same periodicity, and, thus, they can be expressed by a Fourier Series in the form [60]:

$$\mathbf{H}_{\mathbf{k}_z}(\mathbf{r}) \propto \sum \mathbf{c}_{\mathbf{k}_z, m}(x) e^{j\mathbf{k}_z z} e^{jm\frac{2\pi}{\Lambda}z} \quad (2.3.1)$$

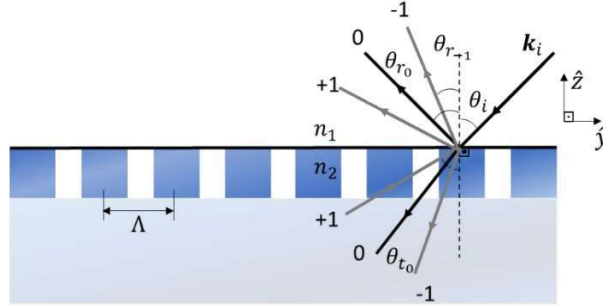
where the term  $\sum \mathbf{c}_{\mathbf{k}_z, m}(x) e^{j\mathbf{k}_z z} e^{jm\frac{2\pi}{\Lambda}z}$  is the Fourier expansion in  $\hat{z}$  direction, with  $\mathbf{k}_z$  being the incidence wavevector component on it,  $\mathbf{c}_{\mathbf{k}_z, m}(x)$  is the  $m^{\text{th}}$  coefficient of the Fourier expansion, where  $m$  is an integer; only a specific combination of  $\mathbf{c}_{\mathbf{k}_z, m}(x)$  will satisfy the solution of the system, which can be found via application of the boundary conditions[60]. The field described by Equation 2.3.1 is usually called a Bloch Mode.

The Bloch Mode is a sum of plane waves, with amplitude and phases determined by its Fourier Series coefficients. The  $\mathbf{k}$ 's component in the  $\hat{z}$  direction of each plane wave is given by the incident field component in the same direction ( $\mathbf{k}_z$ ) plus a multiple of the grating vector ( $\mathbf{G} \triangleq \frac{2\pi}{\Lambda}$ ) (where  $\Lambda$  is the grating period), as:

$$\mathbf{k}_{m_z} = \mathbf{k}_{i_z} \mp m\mathbf{G} \quad (2.3.2)$$

where  $k_{m_z}$  are the wavevector components parallel to the interface of incidence. Equation 2.3.2 is sometimes referred to as the Floquet Condition.

Figure 2-13 – Bragg Law.



The Floquet condition can also be expressed in terms of the angle that each plane wave makes with the axis normal to the grating as illustrated in Figure 2-13; straightforward application of Pythagoras' theorem on the wavevector components of Equation 2.3.2 leads to Equations 2.3.3 [65] – also called Bragg's Law:

$$\Lambda n_1 [\sin(\theta_i) \pm \sin(\theta_{r_m})] = m\lambda \quad (2.3.3a)$$

$$\Lambda [n_1 \sin(\theta_i) \pm n_2 \sin(\theta_{t_m})] = m\lambda \quad (2.3.3b)$$

where  $\lambda$  is the free-space wavelength, and  $\theta_i$  is the incidence angle. Each  $m$  in 2.3.3 represents a diffraction order of the grating and only diffracted waves that satisfy equations 2.3.3 will exist and propagate.

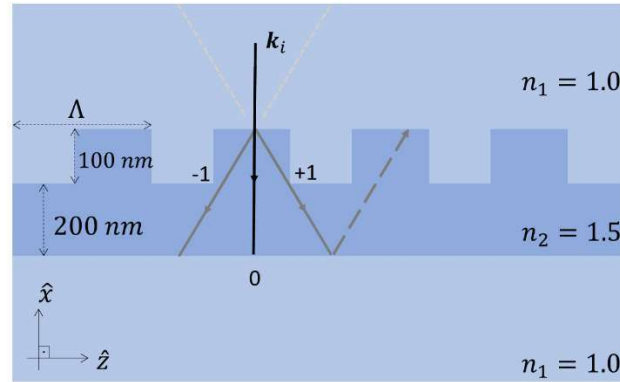
Now, suppose that there is a waveguide below the grating. As discussed in the previous section, the waveguide can be characterized by its propagation constant  $\beta$ , which is the wavevector parallel component in the waveguide. With that in mind, assume that the structure is illuminated by normal incidence ( $\theta_i = 0^\circ$ ), to ease the explanation – as shown in Figure 2-14.

Consider the incident wavelength is such that the diffraction orders  $m = \pm 1$  exist for the transmission (2.3.3b), thus producing a ray with propagation angle given by  $\theta_{\pm 1}$ . In this scenario, two phenomena could happen. First, if  $\theta_{\pm 1}$  does not coincide with the propagation angle of a waveguide mode light propagation will be predominant in the transverse direction and thus the entire structure will act as a thin film, with reflection or transmission spectra similar to a Fabry-Perot interferometer [66]. However, when the  $\theta_{\pm 1}$  coincides with the propagation angle of a waveguide mode, the mode will be excited and light will propagate

horizontally, thus producing a fast phase accumulation, typical of a resonance behaviour, leading to a drastic spectral change both in the transmission and in the reflection.

**Figure 2-14** – Waveguide mode coupling through a grating

Symmetric waveguide with  $n_1 = 1.0$  and  $n_2 = 1.5$ , thickness of 200 nm, with a upper binary grating of period  $\Lambda$ , and height of 100 nm. Assuming that the incidence angle is  $0^\circ$ .



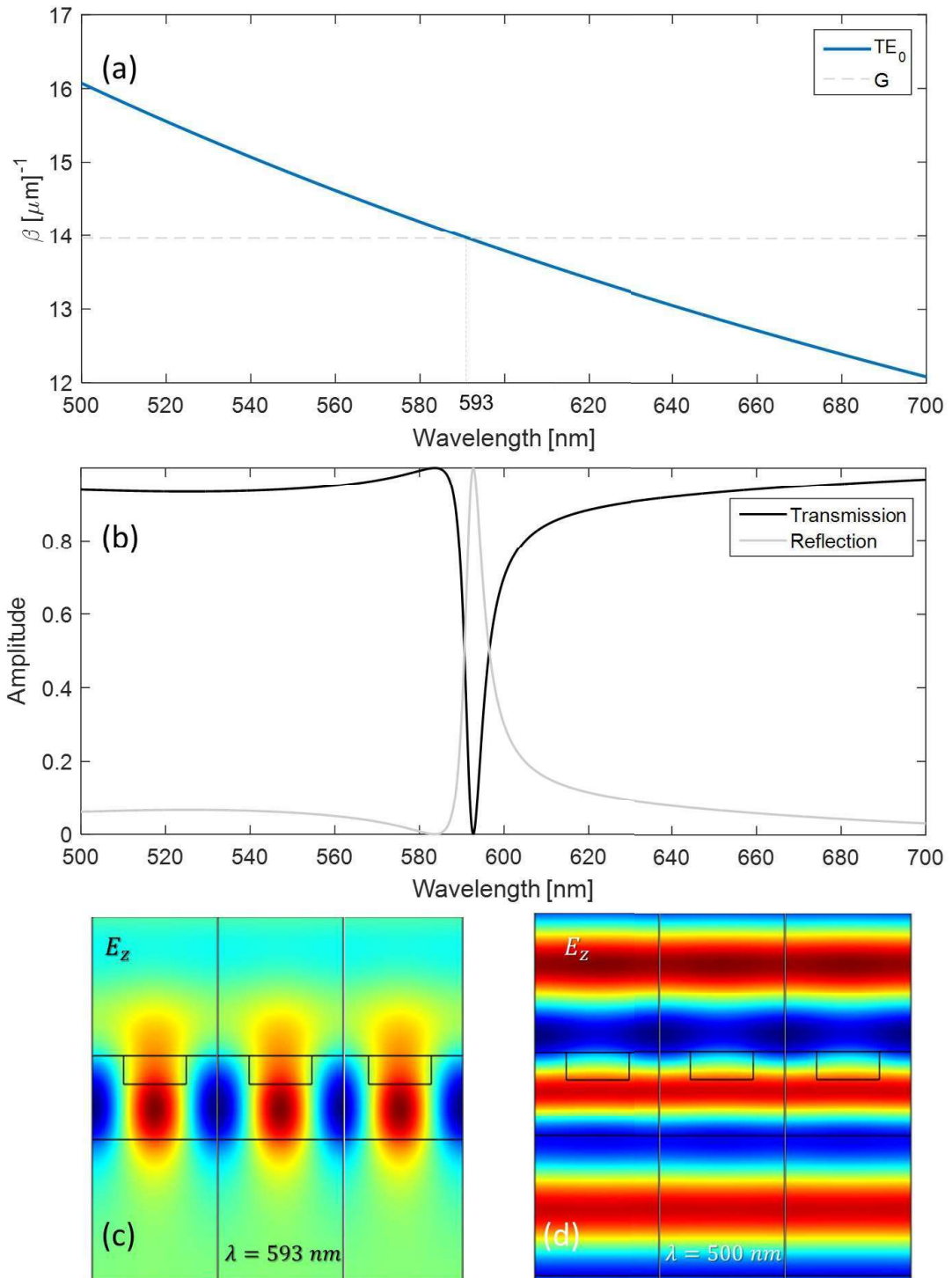
Take the structure of Figure 2-14 as an example; its waveguide supports a single mode in the wavelength range between 500 and 700 nm, for the TE polarization, as shown by dispersion plot in Figure 2-15a. In the example, the grating period is  $\Lambda = 450 \text{ nm}$ , which corresponds to a grating momentum  $\mathbf{G} = 13.96 \text{ } [\mu\text{m}]^{-1}$ ; the position of the grating momentum is marked by the dashed line in Figure 2-15a. The assumption of perpendicular incidence implies that the incident parallel  $k$  vector is null ( $k_{iy} = 0$  in Equation 2.3.2a). Therefore,  $|\mathbf{k}_{1z}| = |\mathbf{k}_{-1z}| = \mathbf{G}$ . The condition for excitation of a mode, on the other hand, is satisfied when one or more of the  $\mathbf{k}_{mz}$  satisfy  $|\mathbf{k}_{1z}| = \beta$ , which means that the mode will be excited for the wavelength that satisfies  $\beta = \mathbf{G}$ . In the dispersion plot of Figure 2-15a, this is the incident wavelength that intercepts the dashed line [67]. The rapid phase accumulation resulting from the excitation of a mode is manifested as a rapid variation on the transmission or reflection spectrum, as shown in Figure 2-15b.

Notice that, for the same reason that gratings couple light into the waveguide, they also couple light out, so the mode is essentially leaky or, in other words, a quasi-guided mode.

Gratings are important in the biosensing scenario because they allow mode coupling from free-space. Although the discussion was made over periodicity in one dimension, the same reasoning can be extended for structures which are periodic in more dimensions, like nanohole arrays, for instance – more information can be found in the review by Cetin et. al. [31]. Besides the dielectric based structure, they are also used in SPR excitation, following the same logic of parallel wavevector matching explained above.

**Figure 2-15** – Dispersion plot and mode coupling

(a) Dispersion of the Mode  $TE_0$  (b) Transmission Spectrum and Reflection Spectra (c) Electric Field at resonance (d) Electric Field out of resonance. The structured simulated in COMSOL via Ports Illumination consisted of 200 nm thick core, superposed with a grating of 100 nm height. The indexes were  $n_1 = n_3 = 1.0$  and  $n_2 = 1.5$ , being the grating consisted of  $n_1$  and  $n_2$  periodic arranged with pitch 450 nm.



The rapid spectral variation resulting from the excitation of a quasi-guided mode resonance forms the basic interrogation mechanism of a guided-mode photonic biosensor. This specific application is discussed in the next section.



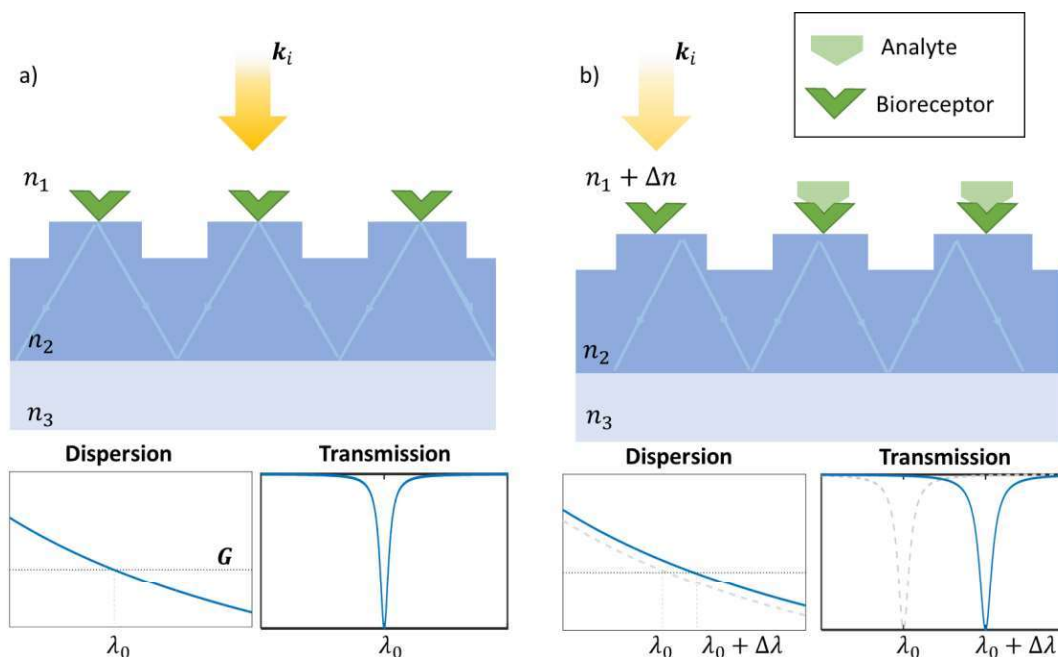
## 2.4 Quasi-guided modes in biosensing

Once the nature of a quasi-guided mode is understood, the goal of this section is to explain how the devices based on this mechanism operate in biosensing. For this, consider the scenario illustrated in Figure 2-16: on the left is displayed almost the same waveguide coupling processes of the previous section, the only difference is the existence of a bioreceptor, whose role is to attach the analyte to the surface. In the absence of analyte, the quasi-guided mode resonant wavelength is  $\lambda_0$ , as shown in the bottom part of Figure 2-16a.

When the analyte bounds with the bioreceptor, the refractive index of the surrounding medium changes by a small amount  $\Delta n$ . However, as it is known from equation 2.2.5, any change in the refractive index induces a change on the propagation condition of the mode inside the waveguide. That is, the propagation angle will no longer be the same, leading to a different propagation constant ( $\beta$ ). Consequently, the dispersion plot varies and the point of interception with the grating momentum – the momentum-matching condition, occurs at other point ( $\lambda_0 + \Delta\lambda$ ), therefore, leading to a resonance shift, as illustrated in Figure 2-16b. The wavelength shift, signals the presence of the analyte, thus constituting the interrogation mechanism of the photonic biosensor. The main parameters that quantify the performance of the sensor are discussed in the next section.

**Figure 2-16** – Resonance shift caused by medium perturbation.

$k_i$  is the incident wavevector,  $n_1$  is the refractive index of the cover region with the bioreceptor,  $n_2$  of the core, and  $n_3$  of the substrate.  $\Delta n$  is the refractive index change caused by the analyte.



## 2.5 Sensing Parameters

Previously, the nature of the most common modes used for biosensing applications were described. It was shown that localized modes can be directly excited by free-space propagation but that they feature broad resonances; guided modes, on the other hand, can display sharper resonances but demand more complex coupling mechanisms; finally, quasi-guided modes retain the advantages of both localized and guided-modes: while it still can be excited from free-space propagation, it also features the sharp resonances associated with guided modes. The goal of the present section is to present the main figures-of-merit used to characterize the resonances.

The Quality-Factor, or Q-Factor, or just Q, is a dimensionless variable defined as the ratio of the time-averaged energy stored in the cavity ( $U/\Delta t$ ) to the energy loss per cycle ( $E_d/T$ ) multiplied by  $2\pi$  [68]:

$$Q \triangleq \omega_0 \frac{U}{P_d} \quad (2.4.1)$$

where,  $U$  is the energy stored,  $P_d$  is the power dissipated per cycle, and  $\omega_0$  is the angular frequency, defined as  $\omega_0 = 2\pi/T$ , which is also the frequency of the mode confined inside the cavity. For the definition 2.4.1, it is possible to derive two other forms for Q [69].

$$Q = \omega_0 \frac{\tau}{2} \quad (2.4.2)$$

$$Q = \frac{\omega_0}{\Delta\omega} = \frac{\lambda_0}{\Delta\lambda_{FWHM}} \quad (2.4.3)$$

In equation 2.4.2,  $\tau$  is the decay time of the mode inside the cavity; this formalism expresses the Q-factor as the number of cycles necessary for the energy inside a cavity to drop by the amount  $e^{2\pi}$ . Equation 2.4.3 is probably the most common form of the Q, and it is derived from the linewidth of the frequency response of the cavity, here  $\Delta\lambda_{FWHM}$  is the fullwidth at half maximum (FWHM) of the Lorentzian line (the Lorentzian line is a consequence of the exponential decay over time).

Although the Q-Factor is defined in terms of a mode confined inside a cavity, its definition can be expanded for other types of mode confinement like waveguides. In this context, the Quality Factor will express how sharp the resonance line of the structure is. As discussed in the previous sections, metallic structures tend to display broader resonances, due to the materials properties, thus having smaller Q, and dielectrics, on the other hand, shows

sharp responses. In a biosensing context, typically higher Q are related to easier detection, since the resonance line shift is more evident. Dielectric based sensors tend to display this characteristic, thanks to their lower absorption.

Another very important parameter in the sensing scenario, perhaps the most significant, is the Sensitivity. The Sensitivity is ratio between the resonance shift ( $\Delta\lambda$ ) and the refractive index variation ( $\Delta n$ ), defined as equation 2.4.5 (with unities nm/RIU):

$$S = \frac{\Delta\lambda}{\Delta n} \text{ [nm/RIU]} \quad (2.4.5)$$

The Sensitivity is typically found in two forms: The Bulk Sensitivity ( $S_B$ ) and the Surface Sensitivity ( $S_S$ ). The  $S_B$  is defined in terms of the refractive index change in the entire cover region, hence the term bulk. The  $S_S$ , on the other hand, is defined in terms of a RI change occurring only on a small thin surface layer, typically of the order dozen nm, which corresponds to the typical analyte size. The sensitivity is strongly dependent on the evanescent field, since it is the interaction between this field and the perturbation that causes the wavelength shift. Therefore, metallic based structures usually display higher  $S_B$  values, and, for the same reason, dielectric sensors based on TM mode excitation are typically more sensitive than TE based ones. Indeed, as it can be seen in Figure 2-10 the electric field is more localized on the cover for TM, and more confined in the core for TE modes.

The last parameter that will be used is a figure-of-merit (FOM) that take into consideration both the Q-Factor and bulk Sensitivity at once. The FOM is defined as the ratio of the  $S_B$  and  $FWHM$ . The use of the  $\Delta\lambda_{FWHM}$  is to take out the influence of the resonance wavelength, because two sensors can display the same line-width but different Q's. This will be relevant in the context of this dissertation for comparison between different systems.

$$\text{FOM} \stackrel{\text{def}}{=} \frac{S_B}{\Delta\lambda_{FWHM}} \quad (2.4.6)$$

### 3 DIELECTRIC VERSUS METALLIC BASED MEDIA SENSORS

The goal of this dissertation is to systematically study and compare the main differences between dielectric and metallic quasi-guided based systems, in terms of their sensing performance and spectral characteristics (Q-Factor). For this, as a starting point, the results of three articles, two from metallic based sensor and one from dielectric, will be reproduced and their main features will be analyzed and compared. The simulations software COMSOL Multiphysics and Lumerical – Finite Difference Time Domain (FDTD), also the Rigorous Coupled Wave Analysis (RCWA) will be used as tools to achieve this goal.

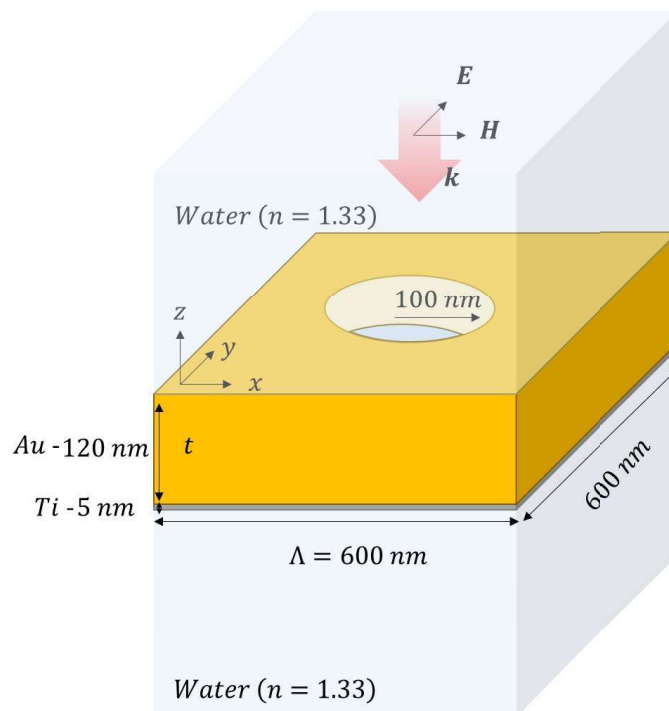
#### 3.1 Nanohole Arrays – Metallic Based Biosensors

Starting with the metallic sensor, Altug’s group have proposed the structure shown in Figure 3-1 for various biosensing utilities [14], [39]–[41]. This sensor is comprised of a thin layer of gold (Au), with thickness ( $t$ ) of 120 nm, patterned with an array of nanoholes (fulling etching the gold layer), with pitch ( $\Lambda$ ) of 600 nm and radius ( $r$ ) of 100 nm, surrounded by an aqueous media. There is a very thin (5 nm) layer of Titanium (Ti) used for membrane placing purposes of the Au layer[37].

**Figure 3-1 - Au Nanoholes structure**

Consisting in a 3D structure, periodic in the  $xz$  and  $yz$  planes, with a unity cell composed by a  $600 \times 600 \times 120 \text{ nm}^3$  Au and a  $600 \times 600 \times 5 \text{ nm}^3$  Ti, with a nanoholes of 200 nm diameter, water as superstrate and substrate.

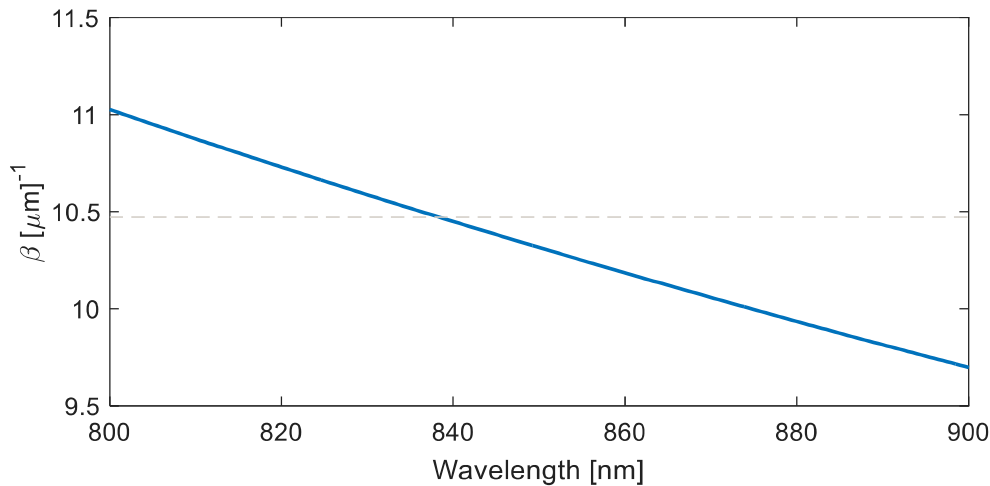
The structure was illuminated normally with the Electric field polarized in the  $y$  direction.



From the dispersion equation for the SPR mode, equation 2.2.8, it is possible to determine the modes supported by this structure. The result shown in Figure 3-2, the dashed line represents the momentum provided by the nanoarray, suggesting that a resonance can be found around 840 nm.<sup>2</sup>

**Figure 3-2** – Dispersion of the SPR.

Blue line represents the dispersion of the SPP mode and Dashed Gray Line the Momentum provided for a symmetric grating of gold and air.



This structure was then simulated with COMSOL using the periodic boundary condition on the parallel boundaries, a Perfect Matched Layer was used on the z direction (normal to the gold layer) and the scattered field was analyzed. The background field used to illuminate the structure was polarized in the y direction, being normally incident. The wavelength ranged from 800 and 950 nm. The transmittance was calculated by integrating the time-average power in a plane on the substrate. The same simulation was performed with Lumerical FDTD and RCWA. For metallic based simulations the RCWA does not have a good convergence, mainly due to the high absorption on the metal. The spectral response is shown in Figure 3-3, the amplitude of the mode was normalized in order to meet the reported results, the maximum value obtained in the simulation was 0.08. This low transmission is characteristic of metallic based structures caused by the absorption of light, but it is typically ignored in the literature, by plotting the spectra in arbitrary units.

<sup>2</sup> Unlike binary gratings the coupling resonance for nanohole arrays structures will be a shifted, depending on the ratio of the constituting materials. For this sensor, the resonance is expected at the right of 840 nm, since there is more gold than air in the layer.

**Figure 3-3** – Transmittance Nanogold array structure.  
The shift on the resonance wavelength is due to the grating size.

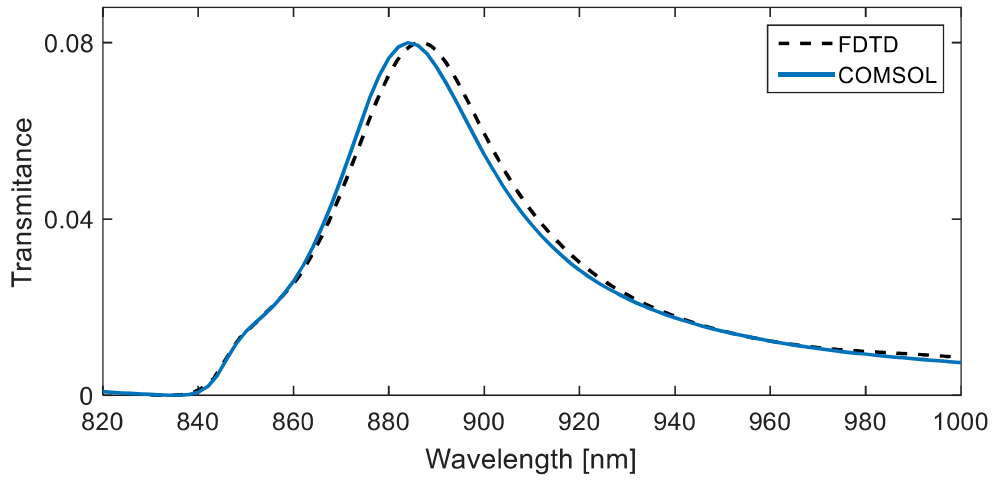


**Figure 3-4** – Field Profile at resonance.

From left to right and top to bottom: Norm of the Electric Field viewed from the Side (YZ plane – the first letter represents the horizontal direction and the second the vertical), Front (XZ) and Top (XY), followed by the Norm of the Magnetic Field in the same order. The brighter regions represent the maxima and the darker the minima.

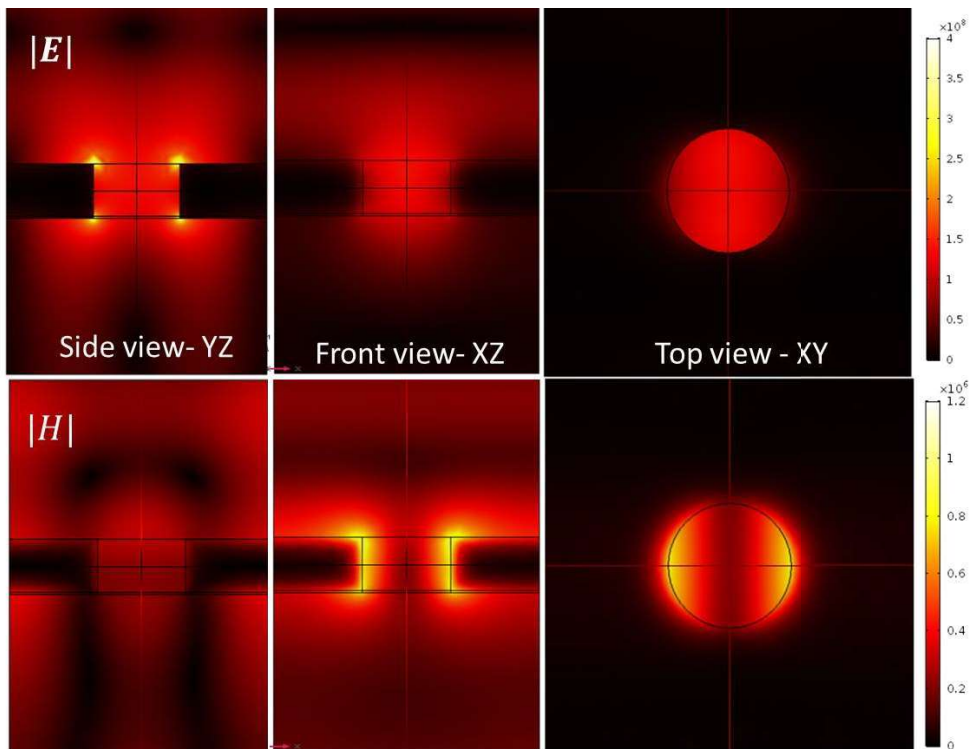


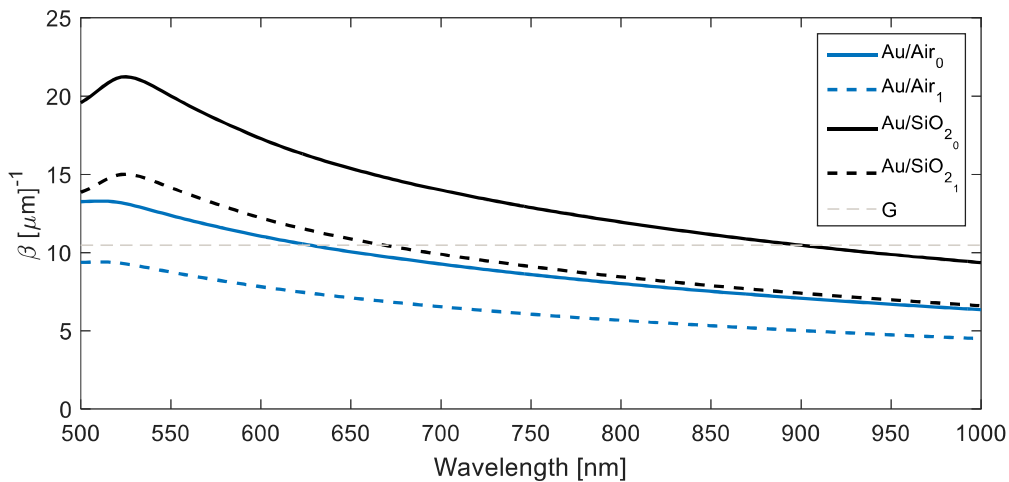
Figure 3-4 shows Field Profile at resonance. A hot spot with a long evanescent tail is noticeable in the corners of the hole for the norm of the Electric Field.

From Figure 3-3, it is possible to find the Q-Factor of the structure, which can also be found using the eigensolver. For this sensor the resonance is at 884 nm and the FWHM of 38 nm (908 – 870 nm), leading to a Q of 23. The Bulk Sensitivity ( $S_B$ ) of this sensor can be

calculated in simulation by varying the refractive index in the cover (upper) region. The  $S_B$  of this sensor is 630 nm/RIU. The Surface Sensitivity ( $S_s$ ), on the other hand, was calculated by varying the refractive index of small volume above the sensor's surface with height of 10 nm. The  $S_s$  of this sensor for this height is 30 nm/RIU. The FOM is then 16,15 RIU<sup>-1</sup>, using equation 2.4.6 considering a S of 630 nm/RIU and  $\Delta_{FWHM}$  of 39 nm.

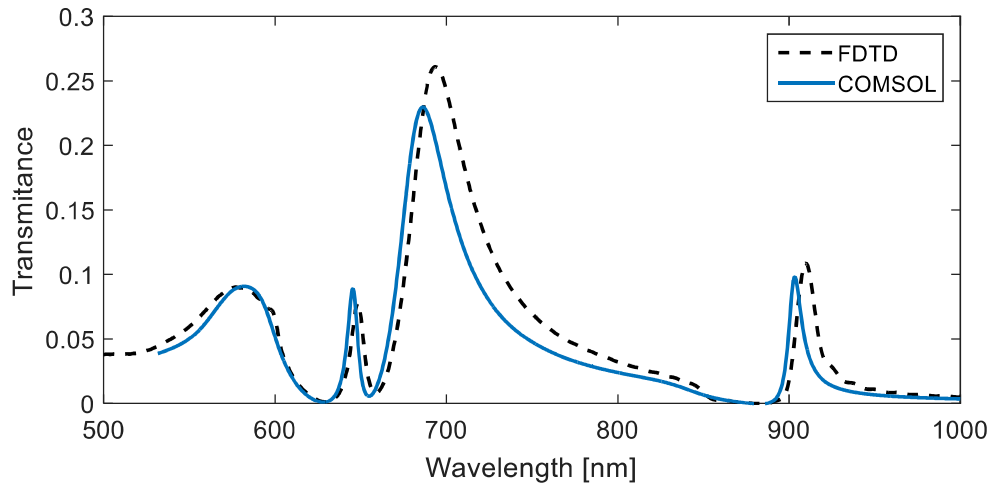
The same research group has proposed another plasmonic sensor, using the same nanohole array on the gold layer [39], shown in Figure 3-1, however in this design glass (SiO<sub>2</sub>) was used as substrate ( $n_{SiO_2} = 1.42$ ), and the cover material was initially set to air ( $n_{air} = 1.00$ ), and then, for the sensitivity calculation, was changed to di-Water ( $n_{H_2O} = 1.33$ ), acetone ( $n_{(CH_3)_2CO} = 1.35$ ), ethanol ( $n_{C_2H_5OH} = 1.36$ ), and isopropanol (IPA) ( $n_{IPA} = 1.37$ ); the Ti layer was removed. The dispersion is shown in Figure 3-5. Notice that, since this structure is asymmetric, there will be modes at the interface between the Gold and the air, in the upper interface, and between the Gold and the Glass, in the lower interface.

**Figure 3-5** – Dispersion of the SPR modes  
The SPR dispersion was calculated via equation 2.2.8



From Figure 3-5, it is expected to find at least three modes when illuminating this structure at normal incidence, since the dashed grey line of the nanohole momentum intercepts the dispersion at three different points: around 640 nm a first order mode is expected in the upper and a second order at the lower, and around 900 nm the first order mode will be excited at the interface between Gold and Glass. All this can be confirmed by inspection of the transmission plot shown in Figure 3-6.

**Figure 3-6** - Transmittance Nanogold array structure



By comparing Figure 3-3 and Figure 3-6, it is clear that the second design has a better transmission, with both higher amplitude and sharper resonances, with  $Q$  of 35, for the mode of the upper interface. However, the presence of the other modes, mainly the one located at 650 nm, spectrally closer to the main resonance 700 nm, could interfere in the detection process. The authors of the paper have then added a layer of Silicon Nitrate ( $\text{Si}_3\text{N}_4$ ) right below the golden layer to get rid of these extras resonances that appeared at the lower interface.

In terms of biosensing performance both sensors were very similar. The  $S_B$  of the present design was calculated and found to be  $S_B = 420 \text{ nm/RIU}$ , even though the paper reports a  $S_B = 671 \text{ nm/RIU}$  (analytical result), and  $S_S = 30 \text{ nm/RIU}$ , value obtained via numerical simulation. On the other hand, since the FWHM is 22 nm, the FOM is 19, greater than the 8.6 of the structure Figure 3-1. This sensor design, which is registered as the patent US 2017/0023476A1[70], has been successfully employed in many applications such as: single cell secretion [37], [40], drug screening [41], and simultaneous detection of two distinct analytes [42].

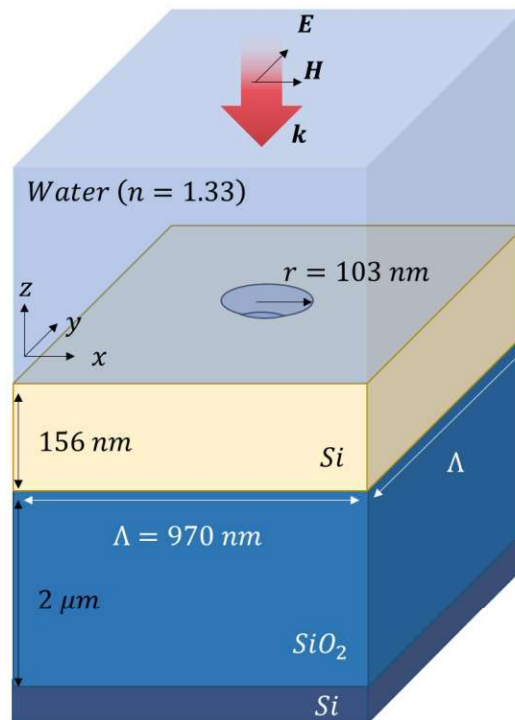


### 3.2 Nanohole Arrays – Dielectric Based Biosensor

Once the main characteristics of the metallic based nanohole biosensors have been illustrated in the previous examples, a similar characterization will be done in this section for sensors based on dielectric media. For this, the sensor design based on Silicon on Insulator (SOI) proposed by Sun et. al. [36] – Figure 3-7 – will be reproduced, and the same parameters analyzed before for plasmonic systems will be calculated for the dielectric sensor.

**Figure 3-7** – SOI nanohole array photonic crystal

It consisted in a 3D structure, periodic in the  $xz$  and  $yz$  planes, with a unity cell compose by a  $970 \times 970 \times 156 \text{ nm}^3$  Crystalline Silicon (c-Si), followed by  $970 \times 970 \times 2000 \text{ nm}^3$  of glass ( $\text{SiO}_2$ ), with a nanoholes of  $206 \text{ nm}$  diameter, water as superstrate, and Amorphous Silicon (a-Si) as substrate. The structure was illuminated normally with the Electric field polarized in the  $y$  direction.

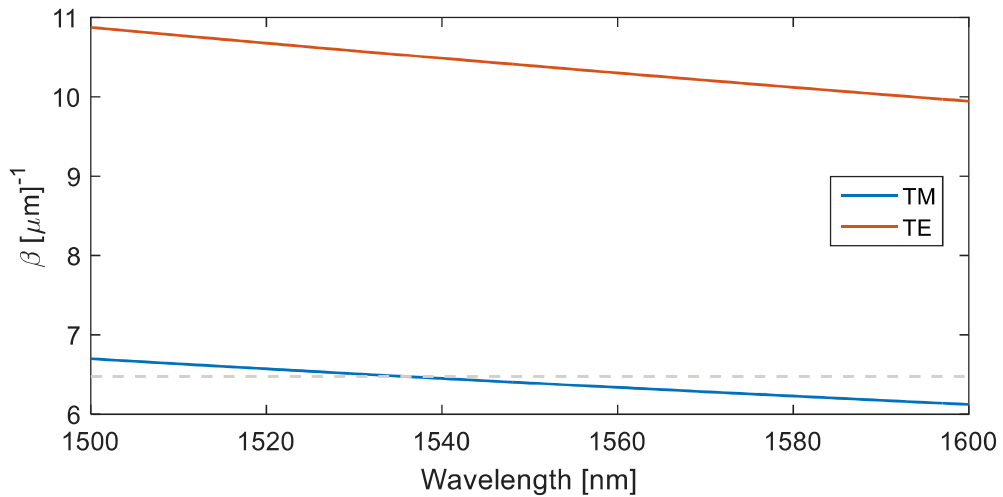


The great challenge of photonic biosensing is to offer a high sensitivity with a good spectral response. The majority of the designs typically show just one of these features. This sensor, on the other hand, provides both a sharp resonance line, with Q-Factor as high as 5000, and fair bulk sensitivity of about  $300 \text{ nm/RIU}$  [36].

Once again, the analysis begins with the dispersion plot in order to have a better understanding of the nature of the modes. Since silicon is absorbing for wavelengths smaller than  $950 \text{ nm}$ , the structure is illuminated with infrared light. In this range ( $1200 - 1600 \text{ nm}$ )

both TE<sub>0</sub> and TM<sub>0</sub> are supported, but just the TM mode will be excited by the nanohole array around 1535 nm, as shown in Figure 3-8.

**Figure 3-8** – Dispersion plot (SOI)



This structure was then simulated in COMSOL using the periodic boundary condition on the parallel boundaries, a Perfect Matched Layer was used on the  $z$  direction, the port setup was used to excite the mode. The incident field was polarized in the  $y$  direction, being normally incident. The wavelength ranged from 1500 and 1600 nm. Notice that the silicon substrate prevents this sensor from operating in transmission mode. The same simulation was performed in RCWA, since this is a semi-analytical approach which demands perform faster than FDTD for dielectric structures. The spectral response is shown in Figure 3-3, displaying a very sharp Fano resonance line with a Q-Factor of 2374 (with a FWHM 0.6 nm).

**Figure 3-9** – Fano resonance of the sensor.

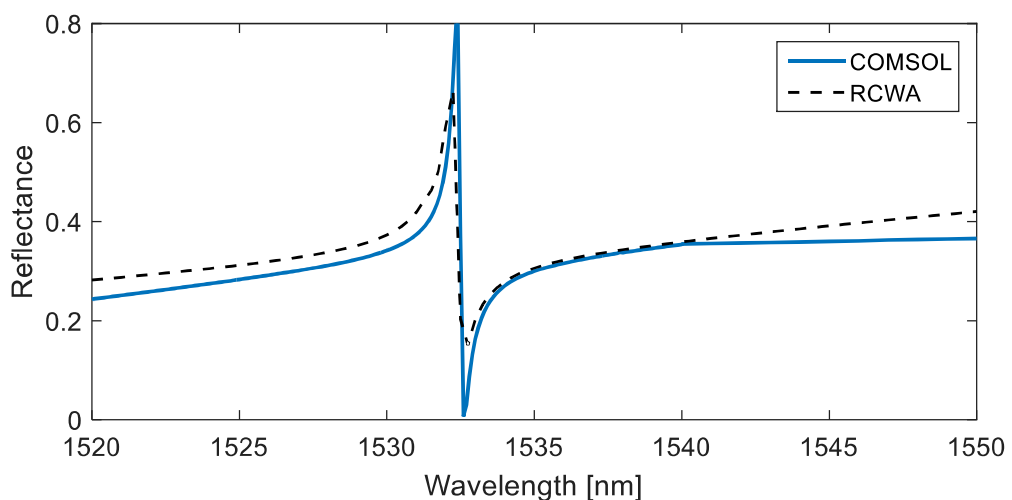
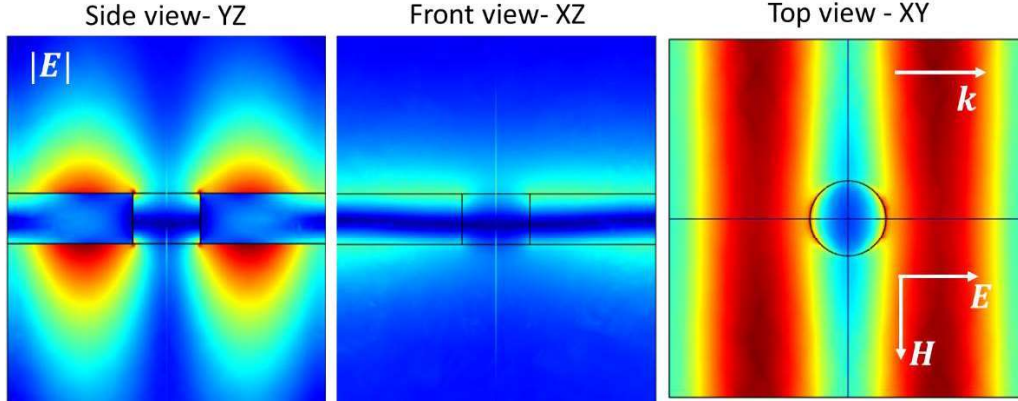


**Figure 3-10** – Field Profile at resonance.

From left to right: Norm of the Electric Field viewed from the Side (YZ plane – the first letter represents the horizontal direction and the second the vertical), Front (XZ) and Top (XY). The reddish regions are maximum values and the blueish represent the minimums. In the top view it is evident the TM likeness of the mode since the propagation direction is parallel to the coupled Electric Field.



From Figure 3-10, it is possible to see (YZ and XY views) the TM like characteristic of the mode, since the Electric Fields is concentrated in the cover and substrate region, with a prominent evanescent tail. By varying the refractive index of the cover region between 1.34 and 1.35, it was found a Bulk Sensitivity of  $S_B = 300 \text{ nm/RIU}$ , the Surface Sensitivity, on the other hand, was  $S_S = 20 \text{ nm/RIU}$  (found by changing the RI of a small volume with 10 nm height). This performance is remarkable, leading to a FOM of  $500 \text{ RIU}^{-1}$ , using the relation 2.4.6 with a S of 300 nm/RIU and  $\Delta_{FWHM}$  of 0.6 nm.

Therefore, although metallic systems win on their overall sensitivities, dielectric based systems can achieve similar results and even offer much better resonance lines. The table below summarizes the main characteristics of the analysed systems

**Table 3** – Sensors Comparison

<i>Sensor</i>	$\lambda_0$ [nm]	$Q$	$S_B$ [nm/RIU]	$S_S$ [nm/RIU]	$FOM$ [RIU] <sup>-1</sup>
<i>Gold/Water</i>	884	23	630	30	16.15
<i>Gold/Air</i>	700	35	420	30	19
<i>SOI</i>	1532	2374	300	20	500

Therefore, the only disadvantages of this SOI sensor is that it is based on reflectance and operates in the infra-red range, which demands a more complex system for detection. In a future work, the author aims to overcome this by proposing a design based on amorphous silicon that operates in transmission and in the mid-infrared.

## 4 DIELECTRIC BIOSENSOR BASED ON a-SI

The previous sections discussed the main characteristics of a photonic biosensor, presenting the physical phenomena involved in their working mechanics, and comparing the performance parameters of both a dielectric and metallic based design. It was shown that although plasmonic devices typically feature higher bulk sensitivities, their FOM are lower than in their dielectric counterparts. Indeed, dielectric sensors can achieve almost the same surface sensitivity as plasmonic devices, but with the advantage of a better Q-factor and spectral responses.

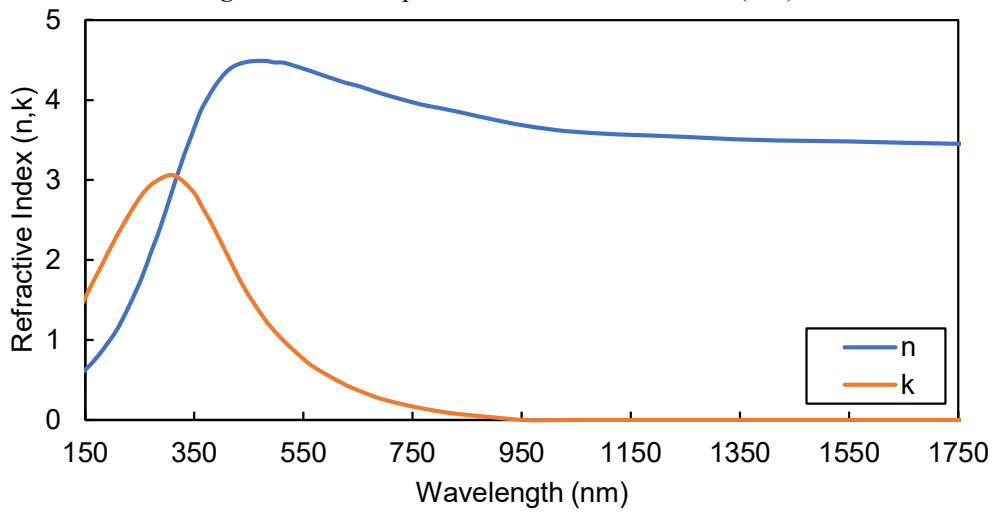
The design proposed by Sun's group [36] has a promising application as a transducer for a Lab on a Chip device. Nevertheless, since it is based on a Silicon-on-Insulator chip, this design cannot operate in transmission [71]. In this scenario, this section investigates a dielectric based quasi-guided mode photonic sensor with performance similar to the SOI one but with the ability of operation both in transmission and in reflection.

### 4.1 Amorphous Silicon (a-Si)

The refractive index of the photonic structures crucially influences their biosensing performance. In principle, a high refractive index is advantageous to confine the light to create the resonances used in probing the surrounding media. Another characteristic to consider is the ease of the fabrication process and the quality of the films, since roughness induces scattering losses that lower the resonances Q-factor.

There are some promising materials such as Titanium Dioxide,  $\text{TiO}_2$ , polycrystalline Silicon, p-Si, crystalline Silicon, c-Si, to name a few; details of these dielectric media can be found in [72]. In this variety of materials, amorphous Silicon, a-Si, was the one chosen for this sensor design, due to its good balance between ease of deposition and high refractive index. As it can be seen on Figure 4-1, the refractive index of the amorphous [73], is virtually constant ( $n = 3.5$ ) and the material is nonabsorbing ( $k = 0$ ) for wavelengths greater than 1,000 nm. This make a-Si a good choice for a sensor operating in the low-infrared part of the spectrum, which is the goal of this work.

**Figure 4-1 – Amorphous Silicon Refractive Index (n, k)**



This research was carried out in a collaboration between USP and the University of York (UK), where the former was responsible for the characterization of the device, design parameters, and numerical simulations, while the latter focused on the fabrication process and experimental characterisation. The fabrication process used hydrogenated amorphous Silicon (a-Si:H), which has optical responses similar to normal a-Si, however the imaginary part of the refractive index is negligible for wavelength greater than 850 nm. Also, the substrate of this wafer was SiO<sub>2</sub>, which in this wavelength range is virtually constant at  $n_{SiO_2} = 1.45$ . [74]

## 4.2 Design of the a-Si Biosensor

Once the material is chosen, the next step is to design the main parameters of the biosensor. In order to do so, it is interesting to start with the waveguide dispersion diagram, as it will provide a better understanding of the mode characteristics. In Figure 4-2, it is shown this plot for a slab waveguide with a-Si core, water ( $n_{H_2O} = 1.33$ ) cover and silica substrate; the thickness of the core was 100 nm. The dashed lines represent the momentum imparted by gratings with periods of 400, 500 and 600 nm.

The period of the grating ( $\Lambda$ ) sets the mode excited by an incoming plane wave; as discussed in the previous sections, the transversal magnetic mode (TM) displays higher sensitivities when compared to the transversal electric (TE) mode, due to the delocalization of the Electric Field from the core. According to dispersion diagram below, a  $\Lambda$  of 500 and of 600 nm, can couple TM modes at the wavelengths of 850 and 1250 nm, respectively; those periods are chosen for this design.

**Figure 4-2 – Dispersion diagram**

Orange line: TE mode dispersion, Blue line: TM mode dispersion. Solid gray line: Momentum provided (G) by a GMR of  $\Lambda = 600 \text{ nm}$ ; Dashed-point gray line: momentum provided by a GMR of  $\Lambda = 500 \text{ nm}$ ; and Dash line momentum provided by a GMR of  $\Lambda = 400 \text{ nm}$

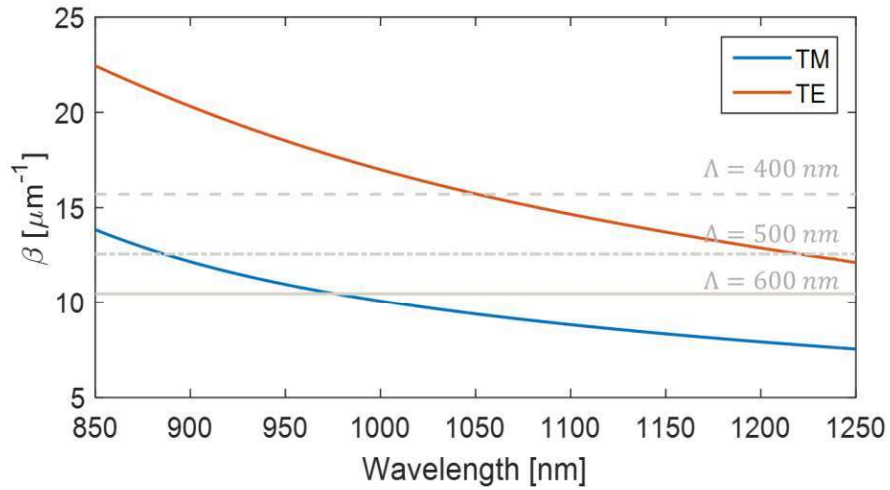
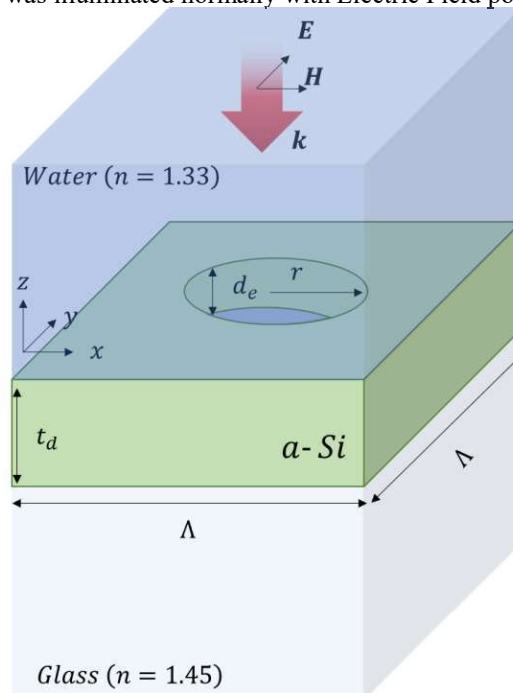


Figure 4-3 shows the biosensor design adopted in this work.  $t_d$  represents the thickness of the core,  $r$  the radius of the hole,  $d_e$  the etching depth, and  $\Lambda$  the period of the structure. Once the dispersion is known, the remaining task is to tune these parameters, in order to obtain the best biosensing performance. As a reference design,  $t_d$  will be set to 100nm,  $d_e$  to 100nm,  $\Lambda$  to 500 nm, and  $r$  to 100 nm, the spectral response is shown in Figure 4-5, next page.

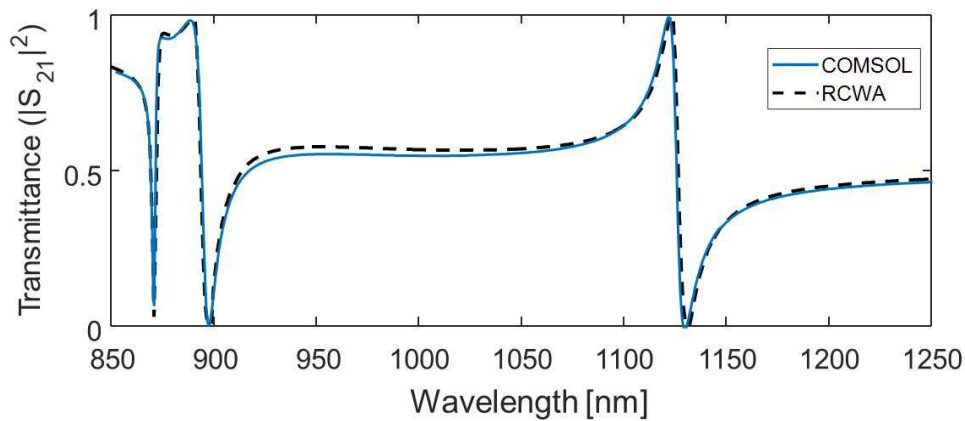
**Figure 4-3 – Biosensor Parameters**

$t_d$  represents the thickness of the core,  $r$  the radius of the hole,  $d_e$  the etching depth, and  $\Lambda$  the period of the structure. The structure was illuminated normally with Electric Field polarized in the y direction.



**Figure 4-4** – Transmittance response

Obtained in COMSOL, blue solid line, and RCWA, dashed black line, via Simulating the structure on Figure 4.3



This structure was then simulated in COMSOL using the periodic boundary condition at the parallel boundaries, a Perfect Matched Layer was used in the  $z$  direction, and the port setup was used to excite the mode. The incident field was polarized in the  $y$  direction, being normally incident. The wavelength ranged from 850 to 1250 nm. The same simulation was performed in RCWA to cross-check the results. The reference design has 3 modes: a TM-like mode localized at 871 nm, a TE-like mode at 1130 nm, (those mode receive the like termination since they are not pure TE or TM modes, they are excited via a Bloch mode with constructive interferes with the momenta required for them) and a pure Bloch mode at 900 nm (where the multiple frequencies components generated by the grating interferes but not in a expected polarization). Their characteristics field profile, and sensing parameters can be seen in Figure 4-5 (a) – (c).

**Figure 4-5 – Biosensor's Fields Profiles**

a) TM-like mode at  $\lambda = 871 \text{ nm}$  b) Pure Block Mode TE like at  $\lambda = 900 \text{ nm}$  c) TE-like mode at  $\lambda = 1130 \text{ nm}$

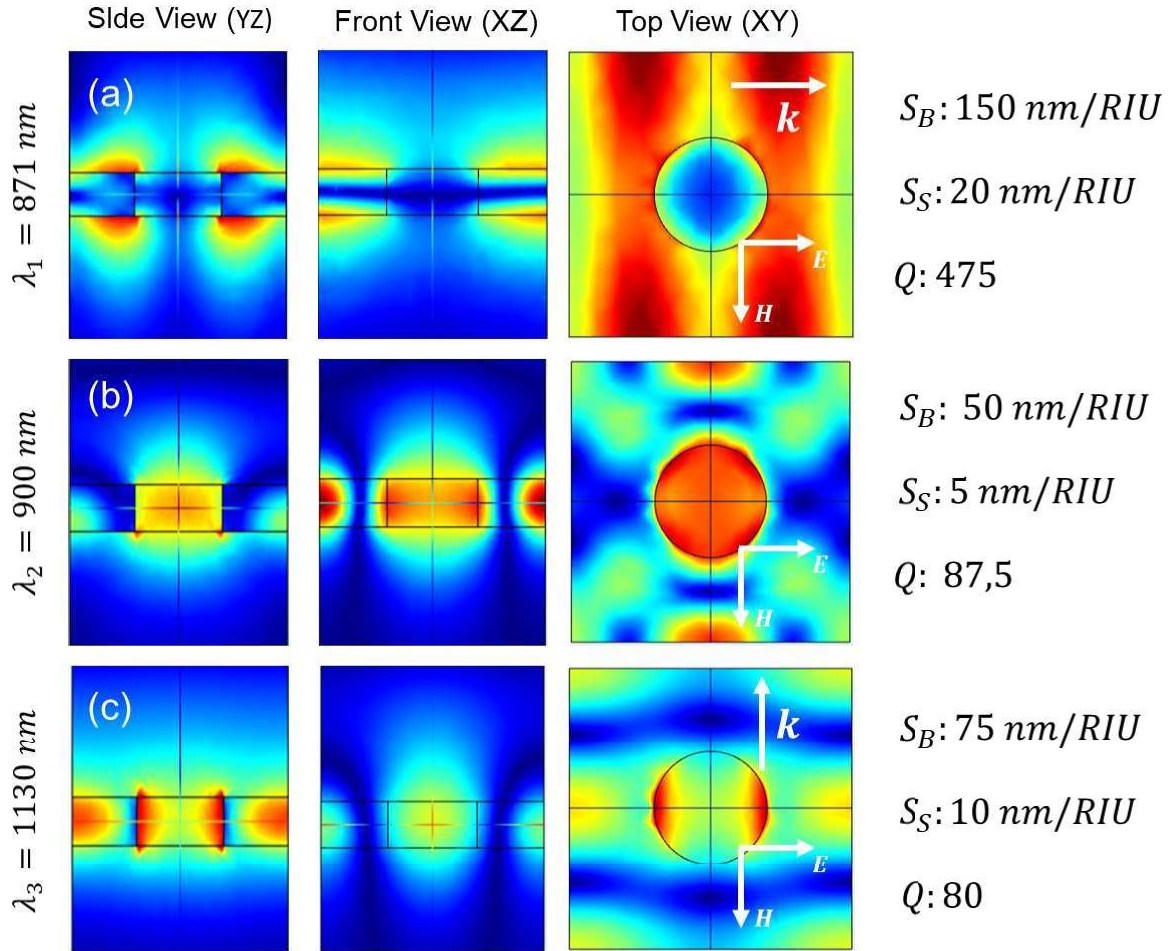


Table 4 compares this reference design with the ones previously studied in this dissertation. The mode with the best performance is the TM-like at 871 nm, which has a bulk sensitivity of 150 nm/RIU, which is in the same range of the SOI design, and a surface sensitivity of 20 nm/RIU, which is comparable to plasmonic sensors. The Q factor was 475, with  $\Delta\lambda_{FWHM} = 1.8 \text{ nm}$ , leading to a FOM of 83 [RIU]<sup>-1</sup>.

**Table 4 – Sensors Comparison**

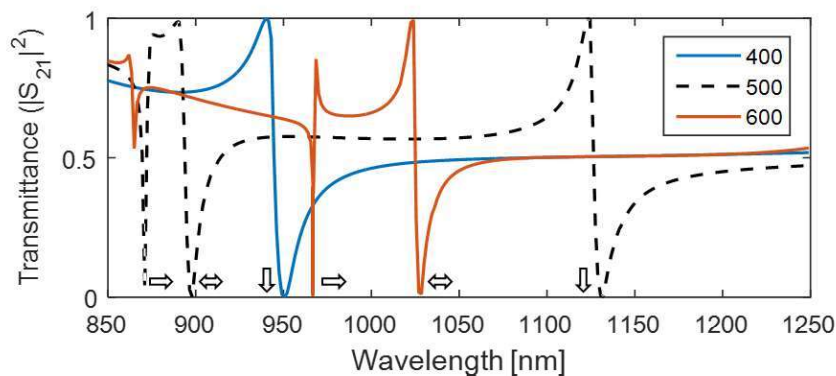
<i>Sensor</i>	$\lambda_0$ [nm]	<i>Q</i>	$S_B$ [nm/RIU]	$S_S$ [nm/RIU]	$FOM$ [RIU] <sup>-1</sup>
<i>Gold/Water</i>	884	23	630	30	16.15
<i>Gold/Air</i>	700	35	420	30	19
<i>SOI</i>	1532	2374	300	20	500
<i>a-Si<sup>(ref)</sup></i>	871	475	150	20	83

In other to understand the influence of each sensor's parameters on the spectral responses and sensing performances, the variables defined in Figure 4-3 were adjusted. In this



scenario, one parameter was manipulated separately while the others were kept fixed. To make it easier to follow the resonances shifts, the following symbols will be used:  $\Rightarrow$  stands TM,  $\Downarrow$  for TE, and  $\Leftrightarrow$  for the pure Bloch. The period  $\Lambda$  was set to 400 nm and 600 nm. In Figure 4-6 the spectral responses for this study are shown; as it was discussed before, the greater the period, the smaller the momentum provided by the excitation; this phenomenon can be seen through the red-shift caused in all modes of the structure; for instance the TE mode located at 1130 nm for  $\Lambda = 500$  nm, moves to 950 nm for  $\Lambda = 400$  nm.

**Figure 4-6 – Influence of  $\Lambda$  on the Spectral Response**



The thickness of the core ( $t_d$ ) directly influences the waveguide dispersion diagram, red shifting the transmission spectrum. Also, as can be seen in Figure 4-7 the thicker is the core, the greater is the transmittance between the pure Bloch and the TE mode, approaching the Fano Resonance to a Lorentzian like curve. The Fabry Perot cavity formed in the a-Si photonic crystal layer has a Lorentzian like shape for the TM mode for  $t = 150$  nm, as it can be seen on Figure 4-9. More in the theory behind it can be found on [75], [76].

**Figure 4-7 – Influence of  $t_d$  on the Spectral Response**

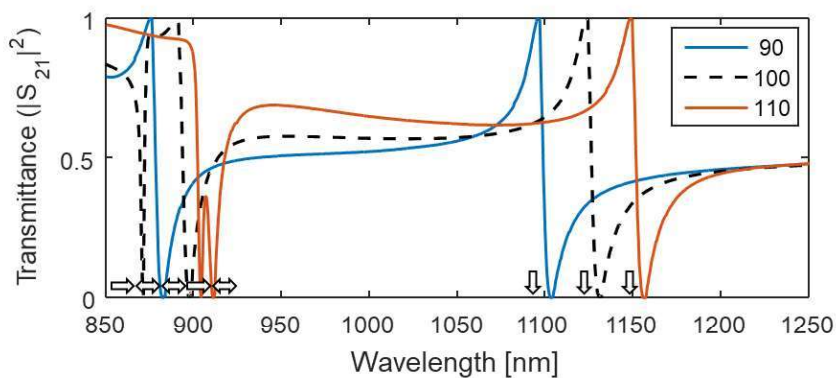
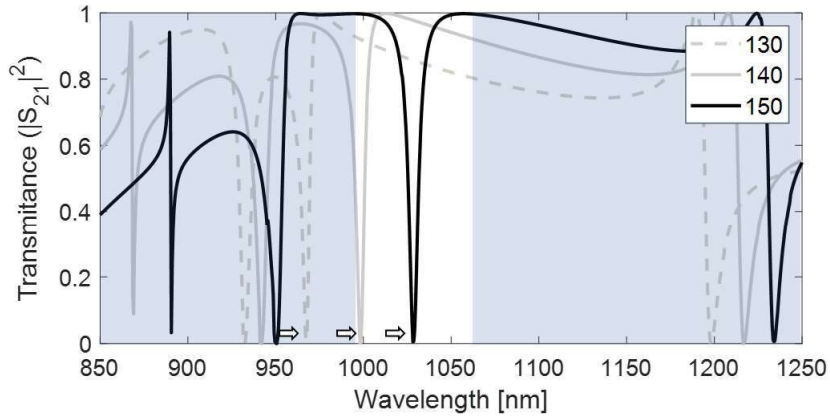
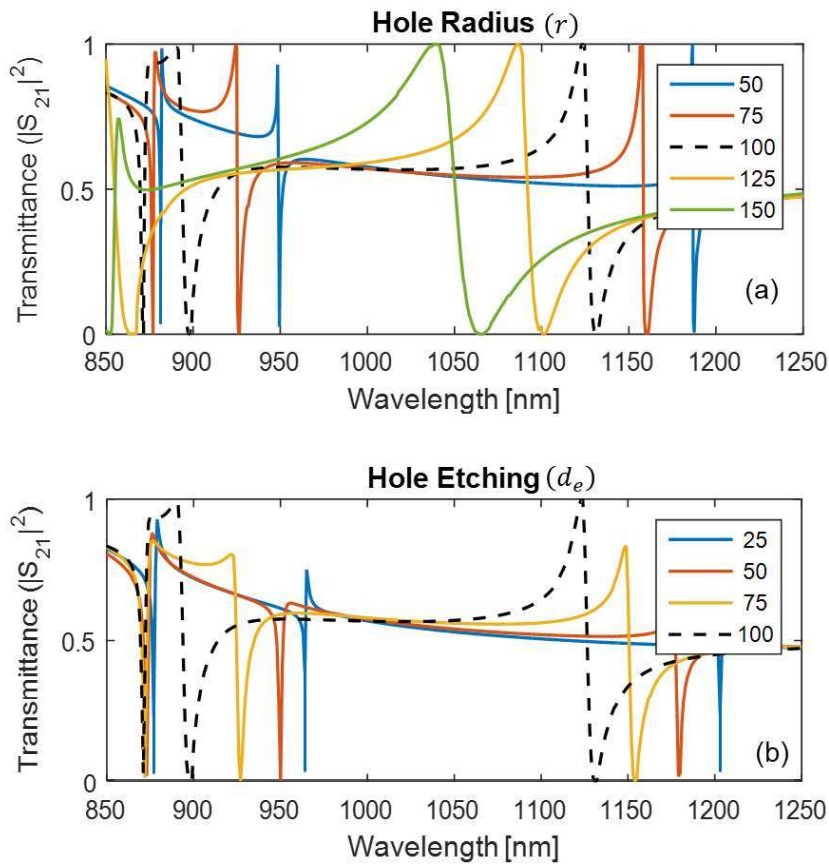


**Figure 4-8** – Influence of  $t_d$  – transition from Fano to Lorentz resonance

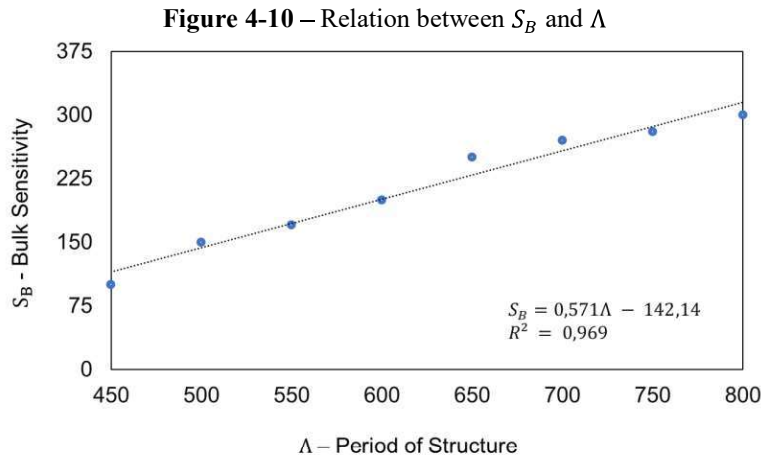


The hole parameters (radius ( $r$ ) and etching depth ( $d_e$ )) have a direct interference on the linewidth of the resonances. This dependence expresses the degree of perturbation of the structure: a smaller radius or shallower etching amounts to a smaller perturbation of the waveguide, thus leading to a longer cavity lifetime, i.e., a larger Q-factor. Notice, however, that a shallow etching leads to weaker resonances. Therefore, it is preferable to control the Q-factor by controlling the hole radius. See Figure 4-9 (a) and (b).

**Figure 4-9** – Influence of the hole parameter  
(a) radius –  $r$  and (b) depth of etching –  $d_e$



To help the analysis of the sensitivity, it is taken the sensitivity of the TM mode located at 871 nm in the Design in Figure 4-5, as reference. In terms of bulk sensitivity (see Table 5), for the parameters studied, there is no clear relation between the terms and  $S_B$ , but for  $\Lambda$ , where  $S_B$  scales with the pitch, for  $\Lambda$  varying from 450 and 800 nm,  $S_B$  can be described by the relation (4.4.1), with a coefficient of determination<sup>3</sup> ( $R^2$ ) of 0,97. See Figure 4-10 for more details.



$$S_B = 0,571 \times \Lambda[\text{nm}] - 142,14 \left[ \frac{\text{nm}}{\text{RIU}} \right] \quad (4.4.1)$$

**Table 5 – Influence of sensor's parameters on Bulk Sensitivity**

	$\Lambda$			$t_d$			$d_e$			$r$		
value [nm]	500	550	600	80	100	120	60	80	100	80	100	120
$S_B$ [nm/RIU]	150	170	200	75	150	100	120	120	150	100	150	150

Based on these results, the design in Figure 4-11 is chosen. It consists of a a-Si dielectric layer with thickness of 100 nm, fully etched by a nanohole array with hole diameter of 100 nm and pitch of 600 nm. Water was used as superstrate and glass as substrate. The spectral response for  $\lambda$  varying from 950 to 1000 nm is shown in Figure 4-12. The coupled mode is a TM mode located at 973 nm, with  $\Delta\lambda_{FWHM} = 0.1$  leading to a Q-Factor of 9730. The  $S_B$  was 200 nm/RIU and  $S_S$  of 25 nm/RIU. The field profile of this mode can be seen on Figure 4-13, once again the TM likeness can be notice via the propagation direction, This operating wavelength was chosen due to the near infrared detector available at the fabrication group [77].

<sup>3</sup> This coefficient varies from 0 to 1 and determines how well a distribution of points can be described by a line.

**Figure 4-11 – Final Design – a-Si nanohole array photonic crystal**

It consisted in a 3D structure, periodic in the  $xz$  and  $yz$  planes, with a unity cell compose by a  $600 \times 600 \times 100 \text{ nm}^3$  amorphous Silicon (a-Si) on a glass ( $\text{SiO}_2$ ) substrate, with a nanoholes of  $100 \text{ nm}$  diameter, water as superstrate. The structure was illuminated normally with the Electric field polarized in the  $y$  direction, with  $\lambda$  varying from  $950 \text{ nm}$  to  $1000 \text{ nm}$ .

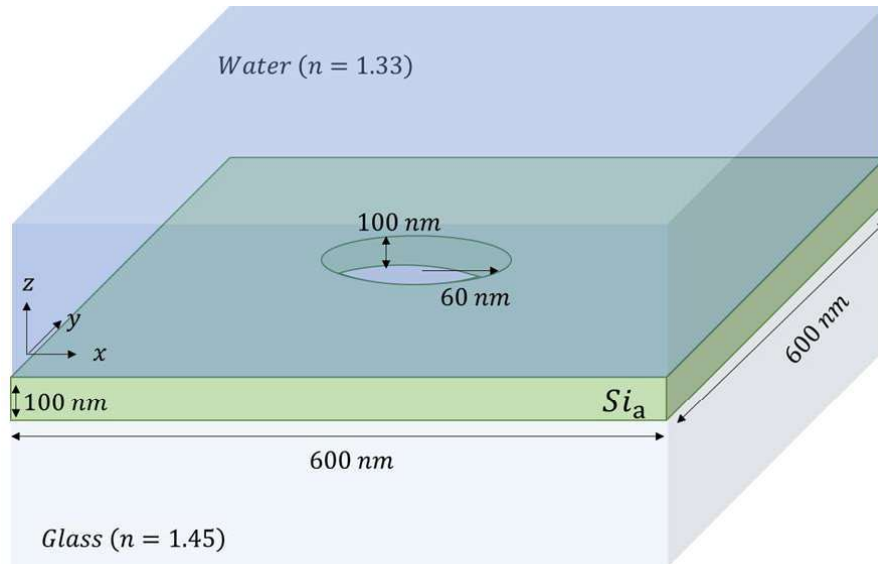


**Figure 4-12 – Transmittance response of the sensor**

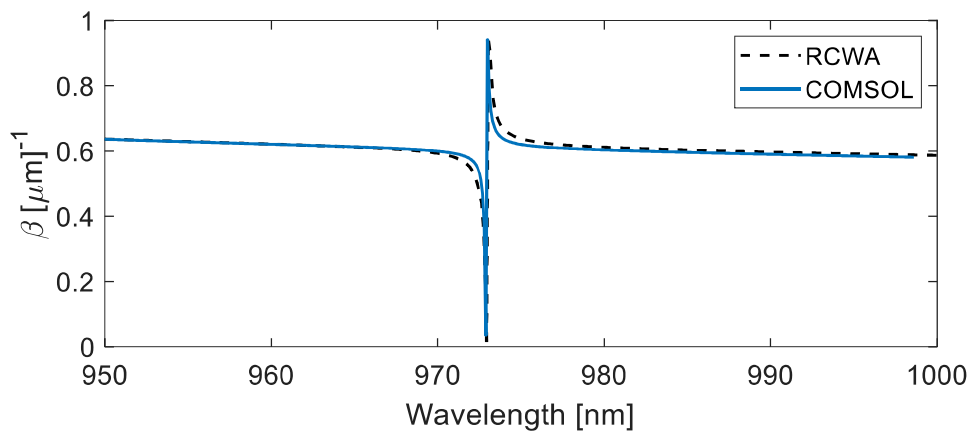
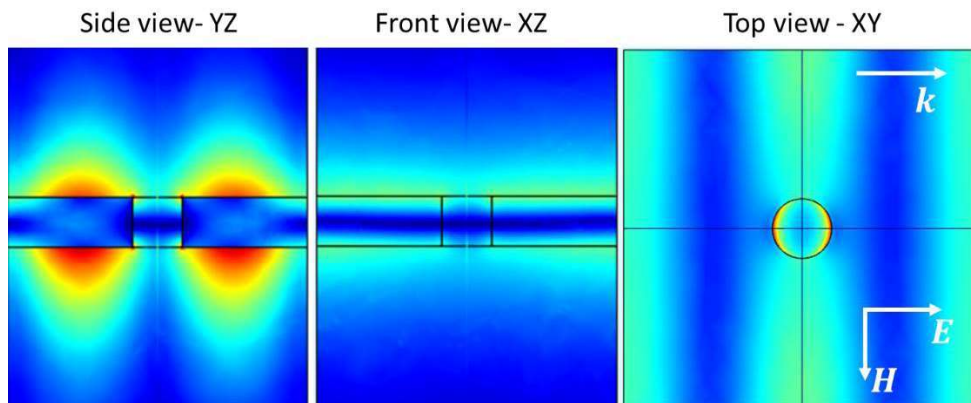


**Figure 4-13 – Field Profile of TM-like Mode**



This sensor performances are finally summarized in Table 6.

**Table 6** – Sensors Comparison

<i>Sensor</i>	$\lambda_0$ [nm]	$Q$	$S_B$ [nm/RIU]	$S_s$ [nm/RIU]	$FOM$ [RIU] <sup>-1</sup>
<i>Gold/Water</i>	884	23	630	30	16.15
<i>Gold/Air</i>	700	35	420	30	19
<i>SOI</i>	1532	2374	300	20	500
<i>a-Si<sup>(ref)</sup></i>	871	475	150	20	83
<i>a-Si<sup>(final)</sup></i>	973	9730	200	25	2000

## 5 CONCLUSIONS

This dissertation offered an overview of the main types of photonic systems employed in biosensing and provided the background for the physical phenomena involved in them as well the main parameters used to measure sensing efficiency. Through the simulation of state-of-the-art designs on metallic and dielectric based sensors, the dissertation presented a systematical comparison between metallic and dielectric sensors [78]. The dissertation concluded that dielectric based sensors have better overall performance, quantified in terms of the FOM. Finally, a novel a-Si based design with FOM two orders of magnitude higher than the plasmonic sensors was presented [77].

## 6 REFERENCES

- [1] Johnson Controls, “Jonhson Controls History”, *Johnson Controls History*, 2018. <https://www.johnsoncontrols.com/about-us/history> (acessado jan. 01, 2019).
- [2] J. Fraden, *Handbook of Modern Sensors*. New York, NY: Springer New York, 2010.
- [3] L. Atzori, A. Iera, e G. Morabito, “The Internet of Things: A survey”, *Computer Networks*, vol. 54, n° 15, p. 2787–2805, 2010, doi: 10.1016/j.comnet.2010.05.010.
- [4] H. Inan *et al.*, “Photonic crystals: emerging biosensors and their promise for point-of-care applications”, *Chemical Society Reviews*, vol. 46, n° 2, p. 366–388, 2017, doi: 10.1039/C6CS00206D.
- [5] M. A. Cooper, “Optical biosensors in drug discovery”, *Nature Reviews Drug Discovery*, vol. 1, n° 7, p. 515–528, 2002, doi: 10.1038/nrd838.
- [6] V. Scognamiglio, F. Arduini, G. Palleschi, e G. Rea, “Biosensing technology for sustainable food safety”, *TrAC - Trends in Analytical Chemistry*, vol. 62, p. 1–10, 2014, doi: 10.1016/j.trac.2014.07.007.
- [7] Analytics Clarivate, “Web of Science”, *Metrics of Biosensing*, 2019. <http://apps.webofknowledge.com/> (acessado ago. 01, 2019).
- [8] C. Karunakaran, R. Rajkumar, e K. Bhargava, “Introduction to Biosensors”, in *Biosensors and Bioelectronics*, n° June, Elsevier, 2015, p. 1–68.
- [9] W. R. Heineman e W. B. Jensen, “Leland C. Clark Jr. (1918–2005)”, *Biosensors and Bioelectronics*, vol. 21, n° 8, p. 1403–1404, fev. 2006, doi: 10.1016/j.bios.2005.12.005.
- [10] B. Raton, L. New, Y. Washington, e T. Vo-Dinh, *Biomedical Photonics Handbook*. 2003.
- [11] L. Bo, N. Claes, e L. Ingemar, “Surface plasmon resonance for gas detection and biosensing”, *Sensors and Actuators*, vol. 4, p. 299–304, 1983, doi: 10.1016/0250-6874(83)85036-7.
- [12] H. M. Kim, M. Uh, D. H. Jeong, H. Y. Lee, J. H. Park, e S. K. Lee, “Localized surface plasmon resonance biosensor using nanopatterned gold particles on the surface of an optical fiber”, *Sensors and Actuators, B: Chemical*, vol. 280, n° June 2018, p. 183–191, 2019, doi: 10.1016/j.snb.2018.10.059.
- [13] S. Kumbhat, R. Gehlot, K. Sharma, U. Singh, e V. Joshi, “Surface plasmon resonance based indirect immunoassay for detection of 17 $\beta$ -estradiol”, *Journal of Pharmaceutical and Biomedical Analysis*, vol. 163, p. 211–216, 2019, doi: 10.1016/j.jpba.2018.10.015.

- [14] X. Li, M. Soler Aznar, A. Belushkin, F. Yesilköy, e H. Altug, “Optofluidic nanoplasmonic biosensor for label-free live cell analysis in real time”, *Plasmonics in Biology and Medicine XV*, n° February 2018, p. 13, 2018, doi: 10.1117/12.2289721.
- [15] E. Luan, H. Shoman, D. M. Ratner, K. C. Cheung, e L. Chrostowski, “Silicon photonic biosensors using label-free detection”, *Sensors (Switzerland)*, vol. 18, n° 10, p. 1–42, 2018, doi: 10.3390/s18103519.
- [16] MarketsandMarkets, “Biosensor Market by Application, Technology, Product, and Geography - Global Forecast”, 2018. <http://bit.ly/biosensorMarketSize> (acessado set. 01, 2019).
- [17] Roayl Society of Chemistry, “Lab on a Chip”, 2019. .
- [18] World Health Organizaion, “Global epidemic surveillance”, 2018. <http://bit.ly/GlobalEpidemicSurveillance>.
- [19] Unesco - Internation Year of Light 2015, “What is Photonics”. <http://www.light2015.org/Home/WhyLightMatters/What-is-Photonics.html> (acessado ago. 01, 2019).
- [20] I. Amiri *et al.*, “Introduction to Photonics: Principles and the Most Recent Applications of Microstructures”, *Micromachines*, vol. 9, n° 9, p. 452, 2018, doi: 10.3390/mi9090452.
- [21] L. M. Lechuga, “Chapter 5 Optical biosensors”, in *Optical Biosensors*, n° 941, 2005, p. 209–250.
- [22] Schmidt+Haensch, “Technical basics refractometry”, 2018. [Online]. Available at: <http://bit.ly/WhatIsRefractometry>.
- [23] A. Leung, P. M. Shankar, e R. Mutharasan, “A review of fiber-optic biosensors”, *Sensors and Actuators, B: Chemical*, vol. 125, n° 2, p. 688–703, 2007, doi: 10.1016/j.snb.2007.03.010.
- [24] G. Pitruzzello e T. F. Krauss, “Photonic crystal resonances for sensing and imaging”, *Journal of Optics*, vol. 20, n° 7, p. 073004, jul. 2018, doi: 10.1088/2040-8986/aac75b.
- [25] V. Amendola, R. Pilot, M. Frascioni, O. M. Maragò, e M. A. Iatì, “Surface plasmon resonance in gold nanoparticles: a review”, *Journal of Physics: Condensed Matter*, vol. 29, n° 20, p. 203002, maio 2017, doi: 10.1088/1361-648X/aa60f3.
- [26] P. Steglich, M. Hülsemann, B. Dietzel, e A. Mai, “Optical Biosensors based on Silicon-On-Insulator Ring Resonator: A Review”, n° January, p. 1–14, 2019, doi: 10.20944/preprints201901.0012.v1.

- [27] J. R. Mejía-Salazar e O. N. Oliveira, “Plasmonic Biosensing”, *Chemical Reviews*, vol. 118, n° 20, p. 10617–10625, 2018, doi: 10.1021/acs.chemrev.8b00359.
- [28] Y. N. Zhang, Y. Zhao, e R. Q. Lv, “A review for optical sensors based on photonic crystal cavities”, *Sensors and Actuators, A: Physical*, vol. 233, p. 374–389, 2015, doi: 10.1016/j.sna.2015.07.025.
- [29] D. Threm, Y. Nazirizadeh, e M. Gerken, “Photonic crystal biosensors towards on-chip integration”, *Journal of Biophotonics*, vol. 5, n° 8–9, p. 601–616, 2012, doi: 10.1002/jbio.201200039.
- [30] A. Csáki, O. Stranik, e W. Fritzsche, “Localized surface plasmon resonance based biosensing”, *Expert Review of Molecular Diagnostics*, vol. 18, n° 3, p. 279–296, mar. 2018, doi: 10.1080/14737159.2018.1440208.
- [31] A.-P. Blanchard-Dionne e M. Meunier, “Sensing with periodic nanohole arrays”, *Advances in Optics and Photonics*, vol. 9, n° 4, p. 891, 2017, doi: 10.1364/AOP.9.000891.
- [32] K. M. Mayer e J. H. Hafner, “Localized Surface Plasmon Resonance Sensors”, *Chemical Reviews*, vol. 111, n° 6, p. 3828–3857, jun. 2011, doi: 10.1021/cr100313v.
- [33] E. Petryayeva e U. J. Krull, “Localized surface plasmon resonance: Nanostructures, bioassays and biosensing-A review”, *Analytica Chimica Acta*, vol. 706, n° 1, p. 8–24, 2011, doi: 10.1016/j.aca.2011.08.020.
- [34] S. Unser, I. Bruzas, J. He, e L. Sagle, “Localized surface plasmon resonance biosensing: Current challenges and approaches”, *Sensors (Switzerland)*, vol. 15, n° 7, p. 15684–15716, 2015, doi: 10.3390/s150715684.
- [35] G. J. Triggs, Y. Wang, C. P. Reardon, M. Fischer, G. J. O. Evans, e T. F. Krauss, “Chirped guided-mode resonance biosensor”, *Optica*, vol. 4, n° 2, p. 229, fev. 2017, doi: 10.1364/OPTICA.4.000229.
- [36] S. Wang, Y. Liu, D. Zhao, H. Yang, W. Zhou, e Y. Sun, “Optofluidic Fano resonance photonic crystal refractometric sensors”, *Applied Physics Letters*, vol. 110, n° 9, 2017, doi: 10.1063/1.4977563.
- [37] X. Li, M. Soler, C. I. Özdemir, A. Belushkin, F. Yesilköy, e H. Altug, “Plasmonic nanohole array biosensor for label-free and real-time analysis of live cell secretion”, *Lab on a Chip*, vol. 17, n° 13, p. 2208–2217, 2017, doi: 10.1039/c7lc00277g.
- [38] A. B. V. Á. Uardado *et al.*, “Hybrid cavity-coupled plasmonic biosensors for low concentration , label-free and selective biomolecular detection .”, *Optics Express*, vol. 24, n° 22, p. 21184–21192, 2016, doi: 10.1364/OE.24.025785.



- [39] A. E. Cetin, D. Etezadi, B. C. Galarreta, M. P. Busson, Y. Eksioglu, e H. Altug, “Plasmonic Nanohole Arrays on a Robust Hybrid Substrate for Highly Sensitive Label-Free Biosensing”, *ACS Photonics*, vol. 2, n° 8, p. 1167–1174, 2015, doi: 10.1021/acsp Photonics.5b00242.
- [40] and H. A. Xiaokang Li, Maria Soler, Crispin Szydzik, Khashayar Khoshmanesh, Julien Schmidt, George Coukos, Arnan Mitchell, “Label-Free Optofluidic Nanobiosensor Enables Real-Time Analysis of Single-Cell Cytokine Secretion”, *Small*, vol. 1800698, p. 1–11, 2018, doi: 10.1002/sml.201800698.
- [41] T. Kilic, M. Soler, N. Fahimi-Kashani, H. Altug, e S. Carrara, “Mining the potential of label-free biosensors for in vitro antipsychotic drug screening”, *Biosensors*, vol. 8, n° 1, p. 1–14, 2018, doi: 10.3390/bios8010006.
- [42] M. Soler, A. Belushkin, A. Cavallini, C. Kebbi-Beghdadi, G. Greub, e H. Altug, “Multiplexed nanoplasmonic biosensor for one-step simultaneous detection of Chlamydia trachomatis and Neisseria gonorrhoeae in urine”, *Biosensors and Bioelectronics*, vol. 94, n° January, p. 560–567, 2017, doi: 10.1016/j.bios.2017.03.047.
- [43] J. P. Monteiro, J. H. de Oliveira, E. Radovanovic, A. G. Brolo, e E. M. Girotto, “Microfluidic Plasmonic Biosensor for Breast Cancer Antigen Detection”, *Plasmonics*, vol. 11, n° 1, p. 45–51, 2016, doi: 10.1007/s11468-015-0016-1.
- [44] J. P. Monteiro *et al.*, “SPR platform based on image acquisition for HER2 antigen detection”, *Nanotechnology*, vol. 28, n° 4, 2017, doi: 10.1088/1361-6528/28/4/045206.
- [45] J. Gomez-Cruz, S. Nair, A. Manjarrez-Hernandez, S. Gavilanes-Parra, G. Ascanio, e C. Escobedo, “Cost-effective flow-through nanohole array-based biosensing platform for the label-free detection of uropathogenic E. coli in real time”, *Biosensors and Bioelectronics*, vol. 106, n° November 2017, p. 105–110, 2018, doi: 10.1016/j.bios.2018.01.055.
- [46] C. Li, G. Bai, Y. Zhang, M. Zhang, e A. Jian, “Optofluidics refractometers”, *Micromachines*, vol. 9, n° 3, p. 1–10, 2018, doi: 10.3390/mi9030136.
- [47] W. Yu, T. Lang, J. Bian, e W. Kong, “Label-free fiber optic biosensor based on thin-core modal interferometer”, *Sensors and Actuators, B: Chemical*, vol. 228, p. 322–329, 2016, doi: 10.1016/j.snb.2016.01.029.
- [48] E. Gorodkiewicz e Z. Lukaszewski, “Recent Progress in Surface Plasmon Resonance Biosensors (2016 to Mid-2018)”, *Biosensors*, vol. 8, n° 4, p. 132, 2018, doi: 10.3390/bios8040132.

- [49] M. Angelopoulou, S. Kakabakos, e P. Petrou, “Label-Free Biosensors Based Onto Monolithically Integrated Onto Silicon Optical Transducers”, p. 1–22, 2018, doi: 10.20944/PREPRINTS201809.0243.V1.
- [50] Z. Zhang *et al.*, “Plasmonic Refractive Index Sensor with High Figure of Merit Based on Concentric-Rings Resonator”, *Sensors*, vol. 18, n° 2, p. 116, jan. 2018, doi: 10.3390/s18010116.
- [51] Y. Sun, Y. Liu, e W. Zhou, “Free-space coupled silicon photonic crystal refractometric membrane sensors”, in *2017 IEEE 14th International Conference on Group IV Photonics (GFP)*, 2017, vol. 2, p. 159–160, doi: 10.1109/GROUP4.2017.8082245.
- [52] Y. Liu, S. Wang, D. Zhao, W. Zhou, e Y. Sun, “High quality factor photonic crystal filter at  $k \approx 0$  and its application for refractive index sensing”, *Optics Express*, vol. 25, n° 9, p. 10536, 2017, doi: 10.1364/OE.25.010536.
- [53] Y. C. Lin, W. H. Hsieh, L. K. Chau, e G. E. Chang, “Intensity-detection-based guided-mode-resonance optofluidic biosensing system for rapid, low-cost, label-free detection”, *Sensors and Actuators, B: Chemical*, vol. 250, p. 659–666, 2017, doi: 10.1016/j.snb.2017.04.187.
- [54] Y. Liu, W. Zhou, e Y. Sun, “Optical refractive index sensing based on high-Q bound states in the continuum in free-space coupled photonic crystal slabs”, *Sensors (Switzerland)*, vol. 17, n° 8, 2017, doi: 10.3390/s17081861.
- [55] C. F. Bohren e D. R. Huffman, “Absorption and Scattering of”, *Light by Small Particles*. p. 209, 1983.
- [56] S. A. Maier, *Plasmonics Fundamentals and Applications*. Bath, UK, 2007.
- [57] S. J. Orfanidis, *Electromagnetic Waves and Antennas*. 2016.
- [58] B. E. A. Saleh e M. C. Teich, *Fundamentals of Photonics*. New York, USA: John Wiley & Sons, Inc., 1991.
- [59] D. J. Griffiths, *Introduction to Electrodynamics, Fourth Edition*. 2012.
- [60] J. D. Joannopoulos, S. G. Johnson, J. N. Winn, e R. D. Meade, *Photonic Crystals - Molding the Flow of Light*. 2018.
- [61] G. Keiser, *Optical Fiber Communicaitons*. 2003.
- [62] S. K. Selvaraja e P. Sethi, “Review on Optical Waveguides”, in *Emerging Waveguide Technology*, vol. 2, InTech, 2018, p. 64.
- [63] H. Mukundan *et al.*, “Waveguide-Based Biosensors for Pathogen Detection”, *Sensors*, vol. 9, n° 7, p. 5783–5809, jul. 2009, doi: 10.3390/s90705783.

- [64] B. A. Prabowo, A. Purwidyantri, e K. C. Liu, “Surface Plasmon Resonance Optical Sensor: A Review on Light Source Technology”, *Biosensors*, vol. 8, n° 3, p. 80, ago. 2018, doi: 10.3390/bios8030080.
- [65] Photonics Research Group - Ghent University, “Periodic Structures”, 2017, p. 1–50.
- [66] Y. Nazirizadeh, *Photonic crystal slabs for low-cost biosensors*. 2010.
- [67] D. Rosenblatt, A. Sharon, e A. A. Friesem, “Resonant grating waveguide structures”, *IEEE Journal of Quantum Electronics*, vol. 33, n° 11, p. 2038–2059, 1997, doi: 10.1109/3.641320.
- [68] J. D. Jackson, *Classical Electrodynamics*. 1962.
- [69] F. Vollmer e L. Yang, “Review Label-free detection with high-Q microcavities: a review of biosensing mechanisms for integrated devices”, *Nanophotonics*, vol. 1, n° 3–4, p. 267–291, jan. 2012, doi: 10.1515/nanoph-2012-0021.
- [70] H. Altug, “US 20170023476A1”, US 20170023476A1, 2017.
- [71] R. Baets *et al.*, “Silicon-on-insulator based nano-photonics: Why, how, what for?”, *2005 IEEE International Conference on Group IV Photonics*, vol. 2005, p. 168–170, 2005, doi: 10.1109/GROUP4.2005.1516441.
- [72] D. G. Baranov *et al.*, “All-dielectric nanophotonics: the quest for better materials and fabrication techniques”, *Optica*, vol. 4, n° 7, p. 814, jul. 2017, doi: 10.1364/OPTICA.4.000814.
- [73] D. T. Pierce e W. E. Spicer, “Electronic Structure of Amorphous Si from Photoemission and Optical Studies”, *Physical Review B*, vol. 5, n° 8, p. 3017–3029, abr. 1972, doi: 10.1103/PhysRevB.5.3017.
- [74] I. H. Malitson, “Interspecimen Comparison of the Refractive Index of Fused Silica\*,†”, *Journal of the Optical Society of America*, vol. 55, n° 10, p. 1205, out. 1965, doi: 10.1364/JOSA.55.001205.
- [75] D. A. Bekele *et al.*, “Signal reshaping and noise suppression using photonic crystal Fano structures”, *Optics Express*, vol. 26, n° 15, p. 19596, 2018, doi: 10.1364/oe.26.019596.
- [76] Y. Yu *et al.*, “Fano resonance control in a photonic crystal structure and its application to ultrafast switching”, *Applied Physics Letters*, vol. 105, n° 6, p. 1–15, 2014, doi: 10.1063/1.4893451.

- [77] D. Conteduca, R. Romão, E. R. Martins, e T. F. Krauss, “All-dielectric nanohole array for high-resolution imaging and enhanced sensitivity”, *2019 Conference on Lasers and Electro-Optics Europe and European Quantum Electronics Conference, CLEO/Europe-EQEC 2019*, p. 6801810, 2019, doi: 10.1109/CLEOE-EQEC.2019.8871666.
- [78] R. R. Franca Soares e E. Rezende Martins, “Systematic comparison between photonic sensors based on dielectrics and metals”, *2019 SBFoton International Optics and Photonics Conference, SBFoton IOPC 2019*, p. 0–4, 2019, doi: 10.1109/SBFoton-IOPC.2019.8910203.